國立交通大學

電子物理學系

碩 士 論 文

石墨烯中時變位能的量子傳輸特性

Time modulated transmission characteristics in a graphene sheet

研 究 生：劉悌鐳

指導教授： 朱仲夏 教授

中 華 民 國 101 年 7 月

中文摘要

電子在石墨烯(Graphene)材料上擁有獨特的介觀傳輸性質，其色散關係(energy dispersion relation)在接近費米能量時呈線性關係，因此電子在這個能量區域的性質如同無質量的狄拉克費米子(massless Dirac fermions)。由相對論的量子理論，無質量的粒子，具有 Klein 穿隧效應(Klein tunneling)，即粒子無法被一時間穩定的位能障 (time-independent potential barrier)所束縛。

本論文分析在石墨烯上電子向時變位能(time-dependent)區垂直入射的傳輸行爲，並透過緊束縛模型(tight-binding model)使得本結果涵蓋非線性色散區域。在低能量區域本結果獲得與前人使用有效哈密頓(effective Hamitonian)的預測一致：Klein 穿隧效應在時變位能作用下時仍然成立，時變的位能亦無法束縛粒子；另外，分析不同位能寬度的傳輸行爲，我們發現了一奇特現象—中央帶再聚集(central band refocusing)效應，即在某些特定的時變位能寬度時，電子只能從中央帶穿隧。在高能量區域我們觀察到不同能谷(inter-valley)之間的散射：電導驟降(dip structure)、旁帶(sideband)特性以及非典型 Fabry-Perot 干涉特性。

我們也探討時變位能對具有能隙的石墨烯(gapped graphene)傳輸的影響，發現同能谷(intra-valley)散射亦能產生電導驟降以及非典型 Fabry-Perot 干涉特性。

Abstract

Electron in graphene has a unique mesoscopic transport property due to its linear dispersion relation when the Fermi energy falls within the low energy regime. The electron behaves as a massless Dirac fermion. Most well-known characteristic of a massless Dirac fermion is the Klein-tunneling, where the particle cannot be blocked or trapped by static barriers.

This thesis focuses on the transport property, in general, and the Klein-tunneling characteristics, in particular, for a graphene acted upon by a time-modulated potential. For the clarity of the physics involved, our consideration is limited to the case of normal incidence. We use tight-binding model for the description of the graphene so that our results cover nonlinear dispersion regime for the electrons. In the low energy regime, we reproduce the Klein-tunneling results in a time-modulating potential case, which has been predicted by Tahir et.al. recently. In addition, we find an exotic central band refocusing phenomenon, where the transmission will be dominated by the central band (the elastic channel) at specific values of the length L of the time-modulated region. This L- periodic phenomenon is explained by a peculiar interference condition that is made possible by the linear energy dispersion relation and the chirality of the particle. Furthermore, we find dip structures in the total transmission in both the high-energy region, and in the low-energy regime of a gapped graphene. These dip structures signify the breakdown of the Klein-tunneling, and is shown to result from coherent hopping to or from the band edge via the emitting or absorbing of photons provided by the time-modulated potential. The band edge has a singular effective density of states as long as the transverse momentum is conserved. Finally, by staying on the dip structures, the total transmission is found to exhibit another L-periodic phenomenon which we can identify as a non-typical Fabry-Perot resonance.

Contents

List of figures

4.1 The graphene sheet is divided into three regions. In region II ($0 \le M \le L$), a time-dependent potential, $V(t) = V_0 \cos(\omega t)$ is presented. The sublattices A and B are denoted as ○ and ●, respectively. The conventional primitive lattice vectors, $\{\boldsymbol{a}_1, \boldsymbol{a}_2\}$, and x-y lattice vectors, $\{\boldsymbol{a}_x, \boldsymbol{a}_y\}$, are labeled. Each lattice site can be represented by

$$m\boldsymbol{a}_1 + n\boldsymbol{a}_2 = (n-m)\boldsymbol{a}_x + (n+m)\boldsymbol{a}_y = M\boldsymbol{a}_x + N\boldsymbol{a}_y . \quad 19$$

4.2 dispersion relation with three typical values of k_y. M_1 and M_2 are the first Brillion zone boundaries in one dimensional momentum space of graphene. 24

4.3 The scattering states constituted by right/left-going states are also exhibited. The right-going states are shown with black color accompanied by bla $-\Delta + \hbar\omega$ arrows, while the left-going states are in gray color with gray left arrows. 25

5.1 The transmission dips appear when the incident Energy is $1\,\hbar\omega$ away from the band edges Δ and $-\Delta$ which have large density of state. L refers to the width of barrier. σ_J indicates the degree of inaccuracy. The arrows show that incident energies $-\Delta + \hbar\omega$ and $\Delta + \hbar\omega$ emit a photon with $\hbar\omega$ and be trapped at valence/conduction band edge. 28

5.2. Shown in the two inserts are blow-ups of the *T-E* curves near the vicinity of the two dip structures in Fig. 5.1. Here $\delta = 10^{-15}\ \hbar\omega$. Whereas the figures show that *T* do not drop to zero at the two dip structures, they confirm that we have found the two minimum *T* values. 29

5.3. The transmission dips appear when the incident Energy is $1\,\hbar\omega$ away from the band edges Δ and $-\Delta$ which have large effective density of state by fixing ky. L refers to the width of barrier. σ_J indicates the degree of inaccuracy. 30

5.4. Shown in the two inserts are blow-ups of the *T-E* curves near the vicinity of the two dip structures in Fig. 5.3. Here $\delta = 10^{-15}\ \hbar\omega$. 31

5.5. The transmission dips appear when the incident Energy is $1\,\hbar\omega$ away from the band edges E_2 which have large effective density of state by fixing ky. L refers to the width of barrier. σ_J indicates the degree of inaccuracy. 32

first-sideband processes are important. The curve shows the dominance of the central band in the transmission. The L-period cannot be explained by the usual Fabry-Perot resonance condition: $2\pi/(q_0^{(2)} - p_0^{(1)}) = 26.5a_x$,where $q_0^{(2)}$, $p_0^{(1)}$ are wavevector-pairs for the elastic channel. It is explained by a non-typical Fabry-Perot resonance that connects wavevector-pairs between the central and the first-sideband channels. 42

Fig. 5.13 stay at dip structure, these series of figures show the transmission is a periodic *L* dependence. 43

Fig. 5.14 Non-typical Fabry-Perot resonance for the case when the system stays at the dip structure, with low incident energy, and the graphene is gapped . The incident energy $E_0 = \Delta + \hbar\omega$ is at an $\hbar\omega$ above the band bottom Δ. The observed physics in Fig. 5.12 remain valid here. The *L*-period is the result of a non-typical Fabry-Perot resonance condition. 44

A.1 Case(a) Energy dispersion fixing $k_y = 0.2(K)$ which means $k_y a_y < \frac{\pi}{2}$. The band bottom is flat. The dashed lines divide energy levels into different scenario, which need to be discussed individually. We will get 4 momentum from Eqn(A.1). In regions $E_{-1} < E < E_1$, $E > E_3$, $E < E_{-3}$ we get 4 complex wave vectors. In regions $E_2 < E < E_3$, $E_{-3} < E < E_{-2}$ we get 2 complex 2 real wave vectors. In regions $E_1 < E < E_2$, $E_{-2} < E < E_{-1}$ we get 4 real wave vectors. We define that if k_x is positive corresponding to the energy region we focus on then we name it K-related wave vector, contrary to K related wave vector if k_x is negative then we name it K'-related wave vector. And we define right-going wave vector as p left-going wave vector as q. Here the valley index was accompany with momentum $p^{(\tau)}$, we define $p^{(1)}, q^{(1)}$ ($p^{(2)}, q^{(2)}$) as $K\,(K')$ valley. X-axis is momentum k_x in unit of $K = \frac{4\pi}{3\sqrt{3}a_0}$;Y-axis is energy in unit $t_0 = 2.8ev$ $E_1 = \sin(k_y a_y)$ $E_{-1} = -E_1, E_{-2} = -E_2, E_{-3} = -E_3$ 46

A.2 Left: Plot momentum $p^{(1)}$ in real(Blue circle) and imaginary(Red cross) part. Fix k_y at 0.2K. Right: Energy dispersion, which used to compare with the left figure. The

red line label the momentum we are discussing. According to energy dispersion plot with red line, the group velocity is always positive. In regions $E > E_2$, $E < E_{-3}$, $E_{-1} < E < E_1$, $p^{(1)}$ is given by evanescent mode.In regions of $E_1 \le E \le E_2, E_{-3} < E < E_{-1}$, $p^{(1)}$ is given by propagating mode. The imaginary part of $p^{(1)}$ become larger as the energy is further away from the band bottom, and become smaller as the energy is closer toward to the band bottom. 47

A.3 Left: Plot momentum $p^{(2)}$ in real(Blue circle) and imaginary(Red cross) part. Fix k_y at 0.2K.

Right: Energy dispersion, which used to compare with the left figure. The red line label the momentum we are discussing. According to energy dispersion plot with red line, the group velocity is always positive. In regions $E < E_{-2}$, $E > E_3$, $E_{-1} < E < E_1$ $p^{(2)}$ is given by evanescent mode. In regions $E_1 \le E \le E_3, E_{-2} < E < E_{-1}$, $p^{(2)}$ is given by propagating mode. The imaginary part of $p^{(2)}$ become larger as the energy is further away from the band bottom, and become smaller as the energy is closer toward to the band bottom. 48

A.4 Energy dispersion fixing $k_y = 0.8(K)$ which means $k_y a_y > \frac{\pi}{2}$. The band bottom is flat. The dashed lines divide energy levels into different scenario, which need to be discussed individually. We will get 4 wave vector from Eqn.(A.1). In regions $E_{-1} < E < E_1$, $E > E_3$, $E < E_{-3}$ we get 4 complex wave vectors. In regions $E_2 < E < E_3$, $E_{-3} < E < E_{-2}$ we get 2 complex 2 real wave vectors. In regions $E_1 < E < E_2$, $E_{-2} < E < E_{-1}$ we get 4 real wave vectors. We define that if k_x is positive corresponding to the energy region we focus on then we name it K-related wave vector, contrary to K related wave vector if k_x is negative then we name it K'-related wave vector. And We define right-going wave vector as p left-going wave vector as q respectively. Here the valley index was accompany with momentum $p^{(\tau)}$, we define $p^{(1)}, q^{(1)}$ ($p^{(2)}, q^{(2)}$) as $K\,(K')$ valley. X-axis is momentum k_x in unit of

Chapter 1

Introduction

Recently, a new kind of material, called graphene has attracted much attention. People did not believe the existence of a single atom thick membrane due to both finite temperature and quantum fluctuations destroy the stability of this material. Not until 2004, did a group from the University of Manchester led by A.K. Geim successfully fabricate this 2D material [1]. Since then, graphene has become a big star in mesoscopic physics. Because of the high electron mobility at room temperature[2] , and the remarkably breaking strength which experimentalists has showed graphene is 200 times greater than steel[3], graphene has been expecting to replace silicon in microelectronic devices.

The transport properties of graphene has paid more and more attention by both theorists and experimentalists, because of the exotic phenomenon , occurred around the corner of Brillouin zone (Dirac cone), Klein paradox[4] which was proposed by M.I. Katsnelson[5]. The reason of existence of this property is due to conservation of chirality.

M. Tahir *et al* [6], who considered the effect of a time-periodic potential on a monolayer graphene and showed that the Klein paradox still holds around Dirac cone. This is due, again, to the conservation of chirality in the presence of the ac field. Using the effective Hamiltonian, this work is limited to the energy regime $|E| < 0.2t_0$, where t_0 is the hopping energy between neighboring atoms.

My fundamental idea of this paper is based on the concept which we employ tight-binding Hamiltonian instead of effective Hamiltonian. The purpose to do so is to discuss the energy level where effective Hamiltonian is not appropriate to use. Furthermore by employing tight-binding Hamiltonian we also can make a discussion about valleytronics which effective Hamiltonian can't tell. We hope there are still some interesting physics within the higher energy level, including inter-valley scattering, Klein paradox breaking, and resonance behavior according to the width of barrier.

Not only employ effective tight-binding Hamiltonian, we also open a global gap right on the Dirac cone to observe the tunneling property in low energy level.

In this work, we have established our formulation systematically. We try this out successfully for

the case of one dimensional tight-binding system in **Chapter 2**. In **Chapter 3** we present the tight-binding model for graphene and establish the conventions and notations to be used in this work. This includes our choice of the primitive lattice vectors that will be most convenient for our wave function matching in **Chapter 4**, AB site identification, and energy spectra as well as tight-binding Hamiltonian, and then we have a brief derivation of effective Hamiltonian. In the end of **Chapter 3**, we have a discussion of Klein tunneling by employing effective Hamiltonian.
Then we will discuss the tunneling property in armchair-edge graphene in **Chapter 4** by using the same way we do in **Chapter 2**. **Chapter 5** gives the results and analyze of the transport property in our system and in the end of this chapter, we will make a conclusion of our work.

Interestingly by using the tight-binding Hamiltonian, Klein paradox still exist while we consider a normal incident wave which the energy is not linear to momentum space.

Chapter 2
Time dependent transport in one-dimensional tight-binding model

In this chapter, we establish, for the tight-binding model, the boundary condition for the time-dependent case. Along this line, we have derived the continuity equation, the current operator, and the conservation of current for the time-dependent case.

2-1 One dimensional time-dependent tight-binding Hamiltonian

In this section, one-dimensional (1D) tight-binding model (TBM) is utilized to discussed the Tien-Gorden model[7]. The system we consider is a 1D chain of atoms (let *a* be the spacing between two nearest atoms) with a time-dependent potential (but spatially-independent), $V_0\cos(\omega t)$, in the whole background. The time-dependent Schrödinger equation (with $\hbar = 1$ henceforward) is

$$\hat{H}|\psi\rangle = i\partial_t|\psi\rangle \tag{2.1}$$

with

$$\hat{H} = \hat{H}_0 + \hat{V}(t) = -t_0\sum_n\left(|n-1\rangle\langle n| + |n+1\rangle\langle n|\right) + V_0\cos(\omega t)\sum_n|n\rangle\langle n|.$$

The general solutions to Eqn. (2.1) is expanded by the eigen-states of $\hat{H}_0$ with the corresponding eigen-energy $E_k = -2t_0\cos(ka)$:

$$|\psi\rangle = \sum_k C_k(t)e^{-iE_kt}|k\rangle \tag{2.2}$$

, where

$$|k\rangle = \tfrac{1}{\sqrt{N}}\sum_n e^{ikna}|n\rangle.$$

Due to the presence of time-dependent potential, the expanding coefficients, $C_k(t)$, in Eqn. (2.2) also depend on time. By Eqn. (2.1), $C_k(t)$ can be further deduced:

$$C_k(t) = c_k e^{-i\frac{V_0}{\omega}\sin(\omega t)} = c_k\sum_m J_m(\tfrac{V_0}{\omega})e^{-im\omega t} \tag{2.3}$$

, where J_m means the 1st-kind of Bessel functions of integer order *m*. Combining Eqns. (2.2) and (2.3):

$$|\psi\rangle = \sum_{k,m} c_k J_m(\tfrac{V_0}{\omega}) e^{-i(E_k + m\omega)t} |k\rangle . \tag{2.4}$$

Eqn. (2.4) is the solution to Tien-Gorden model [7] in 1D TBM.

Before entering next section, it is worth to cast Eqn. (2.1) into a more convenient form. First of all, Eqn. (2.4) is rewritten as

$$|\psi\rangle = \sum_{k,m} c_k J_m(\tfrac{V_0}{\omega}) e^{-i(E_k + m\omega)t} |k\rangle = \tfrac{1}{\sqrt{N}} \sum_{k,m,n} c_k J_m(\tfrac{V_0}{\omega}) e^{-i(E_k + m\omega)t} e^{ikna} |n\rangle = \sum_n f_n(t) |n\rangle \tag{2.5}$$

Project Eqn. (2.1) to the *n*-th orbital, $|n\rangle$, we arrive

$$-t_0 \left(f_{n+1} + f_{n-1} \right) + V_0 \cos(\omega t) f_n = i\partial_t f_n \tag{2.6}$$

Eqn. (2.6) relates the amplitude of the *n*-th orbital, f_n, to those of its nearest neighbor, f_{n+1} and f_{n-1}. Via Eqn. (2.6), the current, continuous equation, and boundary conditions are discussed in the following sections.

2-2 Continuity equation and current

Here, two different approaches are used to obtain the expression for the expectation value of the current. The first route follows the continuity equation from the Schrödinger equation in Eqn. (2.6). The current and its divergence for tight-binding Hamiltonian are identified. On the other hand, the current operator can be defined through the density and the velocity operators. The expectation value of this current operator is consistent with that from the first approach.

Route I. From continuity equation

The probability density on site-*n* is given by $f_n^* f_n / a$. Therefore, from Eqn. (2.6), the continuity equation is

$$\begin{aligned} -\frac{1}{a}\partial_t \left(f_n^* f_n \right) &= -\frac{1}{a}\left(\partial_t f_n^*\right) f_n - f_n^* \frac{1}{a}\left(\partial_t f_n\right) \\ &= \frac{it_0}{a}\left(f_{n+1}^* + f_{n-1}^* \right) f_n - \frac{it_0}{a} f_n^* \left(f_{n+1} - f_{n-1} \right) \\ &= \frac{it_0}{a}\left(\underbrace{f_{n-1}^* f_n}_{\leftarrow} - \underbrace{f_n^* f_{n-1}}_{\rightarrow} + \underbrace{f_{n+1}^* f_n}_{\rightarrow} - \underbrace{f_n^* f_{n+1}}_{\leftarrow} \right) \\ &\equiv \Delta_n(j) \end{aligned} \tag{2.7}$$

The RHS of Eqn. (2.7) is identified as the current divergence, $\Delta_n(j)$, in TBM. There are arrows

below each term in Eqn. 2.7 to indicate the direction of density flux. For example, the term, $f_{n-1}^{*} f_n$, indicates flux from *n* to *n*-1 and thus a left arrow is attached below. From these arrows, $\Delta_n(j)$ is proportional to flux out of site-*n*.

From $\Delta_n(j)$, it is inspired that the current on site-n is related to right going flux:

$$j_n \propto \left(\underbrace{f_n^{*} f_{n-1}}_{\rightarrow} - \underbrace{f_{n-1}^{*} f_n}_{\leftarrow} + \underbrace{f_{n+1}^{*} f_n}_{\rightarrow} - \underbrace{f_n^{*} f_{n+1}}_{\leftarrow} \right) \tag{2.8}$$

To inspect this conjecture, the current in the long-wavelength limit is derived. In this limit, the amplitude, $f_{n\pm1}$, is expanded at as

$$f_{n\pm1} = f(na \pm a) \simeq f_n \pm a(\partial_x f)_n + \frac{a^2}{2}(\partial_x^2 f)_n \tag{2.9}$$

Therefore,

$$\Delta_n(j) \simeq -it_0 a \partial_x \left[f_n^{*} (\partial_x f)_n - (\partial_x f^{*})_n f_n \right] \tag{2.10}$$

Eqn. (2.10) demonstrates the current form in the long wavelength limit:

$$\begin{aligned} j_n &= it_0 a \left[(\partial_x f^{*})_n f_n - f_n^{*} (\partial_x f)_n \right] \\ &= \frac{it_0}{2} \left[\left(f_{n+1}^{*} - f_{n-1}^{*} \right) f_n - f_n^{*} \left(f_{n+1} - f_{n-1} \right) \right] \\ &= \frac{it_0}{2} \left(f_n^{*} f_{n-1} - f_{n-1}^{*} f_n + f_{n+1}^{*} f_n - f_n^{*} f_{n+1} \right) \end{aligned} \tag{2.11}$$

Eqn. (2.11) confirms the conjecture from Eqn. (2.8).

Route II. From current operator

The current operator is defined as

$$\hat{j}_n = \frac{\hat{\rho}_n \hat{v} + \hat{v} \hat{\rho}_n}{2} \tag{2.12}$$

, where $\hat{\rho}_n$ and $\hat{v}$ are the density and velocity operators, respectively. The density operator is related to probability density on site-*n* and has the form:

$$\hat{\rho} = \frac{1}{a} |n\rangle\langle n| \tag{2.13}$$

The velocity operator is derived from the time derivative of position operator, $\hat{x} = a \sum_n n |n\rangle\langle n|$:

$$\hat{v} = \frac{d\hat{x}}{dt} = \frac{\left[\hat{x}, \hat{H} \right]}{i} = \frac{at_0}{i} \sum_n \left(|n-1\rangle\langle n| - |n+1\rangle\langle n| \right) \tag{2.14}$$

The commutator in Eqn. (2.14) is evaluated via the Hamiltonian defined in Eqn. (2.1):

$$\left[\hat{x},\hat{H}\right]=at_0\sum_n\left(\left|n-1\right\rangle\left\langle n\right|-\left|n+1\right\rangle\left\langle n\right|\right)$$

Therefore, the current operator is reached:

$$\hat{j}_n=\frac{it_0}{2}\left[\left|n\right\rangle\left\langle n-1\right|-\left|n-1\right\rangle\left\langle n\right|+\left|n+1\right\rangle\left\langle n\right|-\left|n\right\rangle\left\langle n+1\right|\right] \tag{2.15}$$

The expectation value of $\hat{j}_n$ with $\left|\psi\right\rangle=\sum_n f_n(t)\left|n\right\rangle$, recovers Eqn. (2.11). This ensures the two routes are consistent.

$$\left\langle\psi\right|\hat{j}_n\left|\psi\right\rangle=\frac{it_0}{2}\left(f_n^*f_{n-1}-f_{n-1}^*f_n+f_{n+1}^*f_n-f_n^*f_{n+1}\right) \tag{2.16}$$

2-3 Boundary conditions and scattering states

With the preliminary in **Secs. 2-1** and **2-2**, it is ready for the system of a time-dependent potential barriers in a 1D atomic chain. **Fig. 2.1** displays the system that the barrier separates the space into three regions. The potential is presence in the region *II* with $0\le n\le L$ as shown in **Fig. 2.1**. The boundary conditions between the wave functions in different regions are discussed in this section.

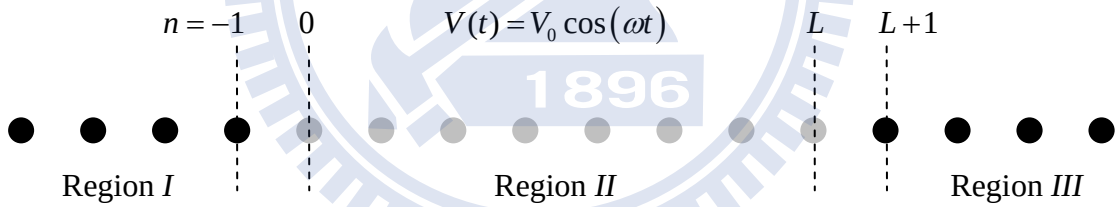

Fig. 2.1 The time-dependent potential barrier is presence from site-0 to site-*L*. The system is divided into three regions: Region *I* ($n\le -1$), Region *II* ($0\le n\le L$), and Region *III* ($L<n$).

For the presence of potential barrier, the Schrödinger equation (Eqn. (2.6)) is separated into three equations:

$$-t_0\left[f_{n-1}(t)+f_{n+1}(t)\right]=i\partial_t f_n(t) \qquad n\le -1 \qquad (2.17\text{ a})$$

$$-t_0\left[f_{n-1}(t)+f_{n+1}(t)\right]+V_0\cos(\omega t)\,f_n(t)=i\partial_t f_n(t) \qquad 0\le n\le L \qquad (2.17\text{ b})$$

$$-t_0\left[f_{n-1}(t)+f_{n+1}(t)\right]=i\partial_t f_n(t) \qquad n\ge L+1 \qquad (2.17\text{ c})$$

Note the constraints imposed in each equation in Eqn. (2.17). For example, Eqn. (2.17 a) holds only for those $n\le -1$. To derive the boundary conditions, ***the auxiliary functions***, $F_n^{(I)}$, $F_n^{(II)}(t)$ and

$F_n^{(III)}(t)$ are introduced by the following Schrödinger equations without any spatial constraint:

$$-t_0\left(F_{n-1}^{(I)}+F_{n+1}^{(I)}\right)=i\partial_t F_n^{(I)} \tag{2.18 a}$$

$$-t_0\left(F_{n-1}^{(II)}+F_{n+1}^{(II)}\right)+V_0\cos(\omega t)F_n^{(II)}=i\partial_t F_n^{(II)} \tag{2.18 b}$$

$$-t_0\left(F_{n-1}^{(III)}+F_{n+1}^{(III)}\right)=i\partial_t F_n^{(III)} \tag{2.18 c}$$

By Eqns. (2.17) and (2.18), the auxiliary functions are further required that

$$\begin{aligned} F_n^{(I)} &= f_n \qquad n\le -1 \\ F_n^{(II)} &= f_n \qquad 0\le n\le L \\ F_n^{(III)} &= f_n \qquad n\le L+1 \end{aligned} \tag{2.19}$$

At boundary $n=-1$, Eqns. (2.17 a) and (2.18 a) read:

$$-t_0\left(f_0+f_{-2}\right)=i\partial_t f_{-1}, \tag{2.20}$$

$$-t_0\left(F_0^{(I)}+F_{-2}^{(I)}\right)=i\partial_t F_{-1}^{(I)} \tag{2.21}$$

Compare with Eqns. (2.19), (2.20), and (2.21) leads to the boundary condition for the auxiliary functions in regions *I* and *II* at $n=0$:

$$F_0^{(I)}=f_0=F_0^{(II)} \tag{2.22 a}$$

Similar procedures will lead to other boundary conditions and they are listed below with derivations omitted:

$$F_{-1}^{(II)}=f_{-1}=F_{-1}^{(I)} \tag{2.22 b}$$

$$F_L^{(III)}=f_L=F_L^{(II)} \tag{2.22 c}$$

$$F_{L+1}^{(II)}=f_{L+1}=F_{L+1}^{(III)} \tag{2.22 d}$$

For the auxiliary functions and the boundary conditions between them, the wave function, $f_n(t)$, is ready to be solved. It usually takes two steps: write down the general forms of the auxiliary functions from Eqns. (2.18) individually, then impose the boundary conditions from Eqn. (2.22) that $f_n(t)$ is the combination of $F_n^{(I)}$, $F_n^{(II)}$ and $F_n^{(III)}$ in three regions.

At the first stage, the general forms for $F_n^{(I)}$, $F_n^{(II)}$ and $F_n^{(III)}$ are inspired by Eqns. (2.4) and (2.5):

$$F_n^{(I)}(t)=\tfrac{1}{\sqrt{N}}\sum_k c_k^{(I)}e^{-iE_k t}e^{ikna}=\tfrac{1}{\sqrt{N}}\sum_\varepsilon\left(c_{p_\varepsilon}^{(I)}e^{ip_\varepsilon na}+R_\varepsilon e^{iq_\varepsilon na}\right)e^{-i\varepsilon t} \tag{2.23 a}$$

$$F_n^{(II)}(t)=\frac{1}{\sqrt{N}}\sum_{k,m}c_k^{(II)}J_m(\frac{V_0}{\omega})e^{-i(E_k+m\omega)t}e^{ikna}=\frac{1}{\sqrt{N}}\sum_{\varepsilon,m}\left(A_\varepsilon e^{ip_\varepsilon na}+B_\varepsilon e^{iq_\varepsilon na}\right)J_m(\frac{V_0}{\omega})e^{-i(\varepsilon+m\omega)t} \quad (2.23\text{ b})$$

$$F_n^{(III)}(t)=\frac{1}{\sqrt{N}}\sum_{k}c_k^{(III)}e^{-iE_kt}e^{ikna}=\frac{1}{\sqrt{N}}\sum_{\varepsilon}T_\varepsilon e^{ip_\varepsilon na}e^{-i\varepsilon t} \quad (2.23\text{ c})$$

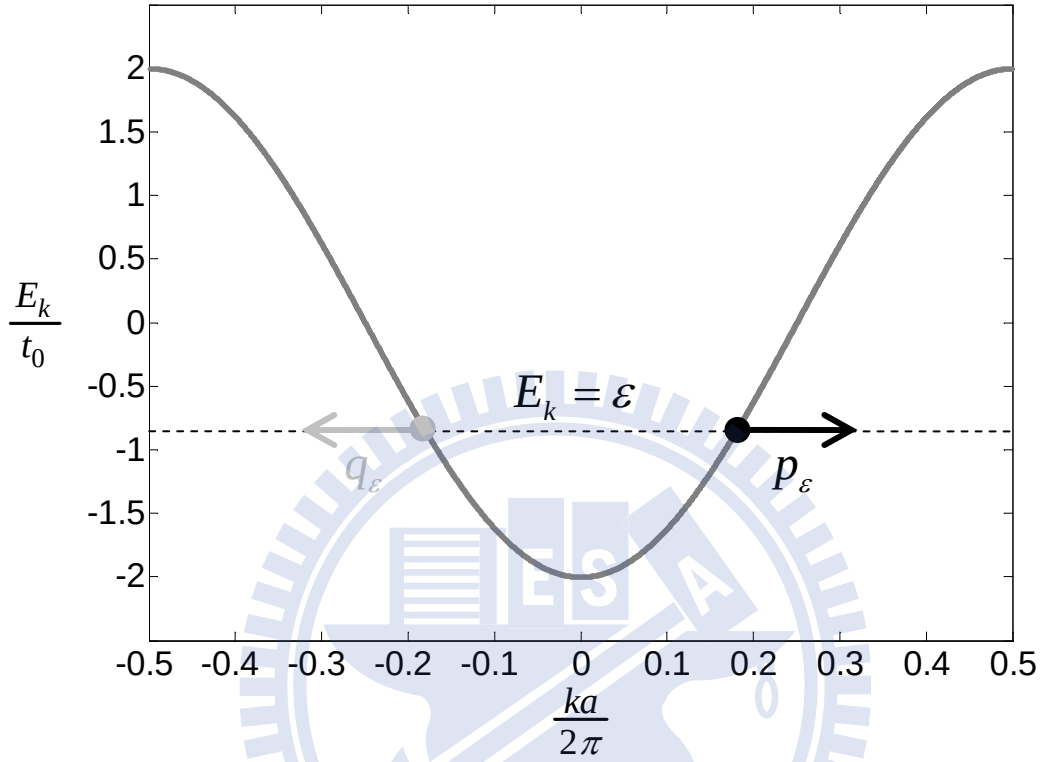

Fig. 2.2 The dispersion of 1D TBM. The right/left-going wave vectors are illustrated by blacked/grayed circles individually.(at certain possible energy)

Note the summation over *k* in Eqns. (2.23) are transformed into energy-sum which sum over all possible energy. The p_ε and q_ε are the right-going-*k* and left-going-*k* corresponding to energy, ε. The right/left-going-k are in the sense that the group velocities are right/left-going. **Fig. 2.2** is the dispersion of $\hat{H}_0$ that p_ε and q_ε is easily read out. The initial condition is already imposed that the waves are incident from region *I*. Hence, the right-going scattering states are looked for. In **Fig. 2.3**, the scattering states composed by these right/left-going Bloch wave vectors, *k* are exhibited in individual regions. The procedures to determine these *k* are discussed in **Appendix A**.

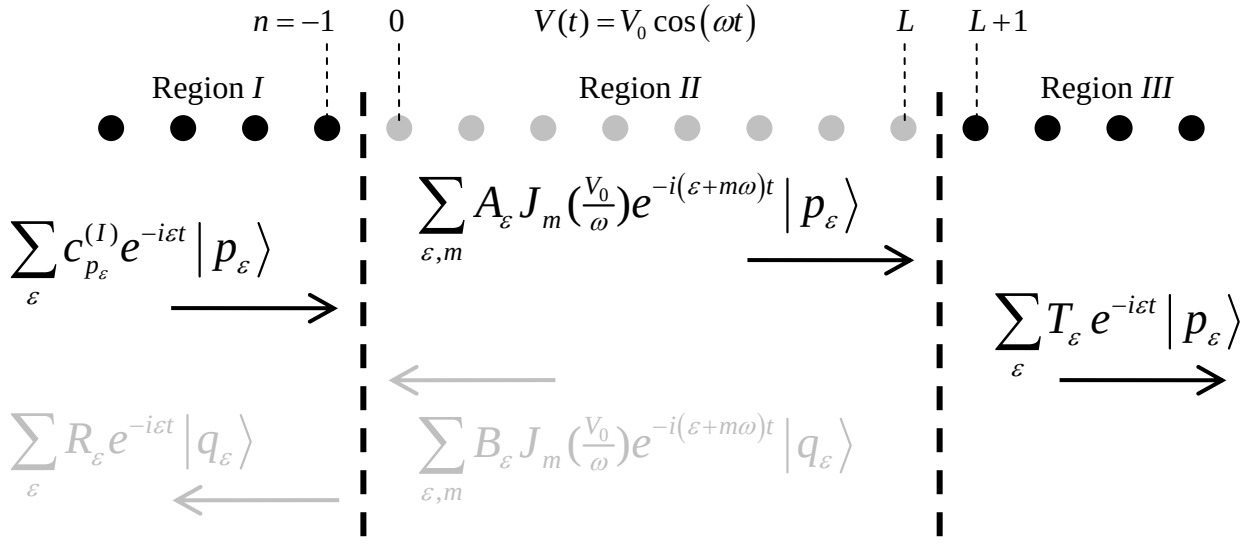

Fig. 2.3 The scattering states constituted by right/left-going states are also exhibited. The right-going states are shown with black color accompanied by black right arrows, while the left-going states are in gray color with gray left arrows.

For the 2nd stage, the boundary conditions require these auxiliary functions are equal for all time at the boundaries. For example, from Eqns. (2.22 a), (2.23 a) and (2.23 b):

$$\sum_{\varepsilon}\left(c^{(I)}_{p_\varepsilon}+R_\varepsilon\right)e^{-i\varepsilon t}=\sum_{\varepsilon,m}\left(A_\varepsilon+B_\varepsilon\right)J_m(\tfrac{V_0}{\omega})e^{-i(\varepsilon+m\omega)t} \tag{2.24}$$

Let $\varepsilon=\varepsilon_0+s\omega$ with $s\in\mathbb{Z}$, and rearrange the summation as:

$$\begin{aligned}\sum_{\varepsilon_0,s}\left(c^{(I)}_{p_{\varepsilon_0+s\omega}}+R_{\varepsilon_0+s\omega}\right)e^{-i(\varepsilon_0+s\omega)t}&=\sum_{\varepsilon_0,m,s}\left(A_{\varepsilon_0+s\omega}+B_{\varepsilon_0+s\omega}\right)J_m(\tfrac{V_0}{\omega})e^{-i[\varepsilon_0+(m+s)\omega]t}\\&=\sum_{\varepsilon_0,m,s}\left(A_{\varepsilon_0+m\omega}+B_{\varepsilon_0+m\omega}\right)J_{s-m}(\tfrac{V_0}{\omega})e^{-i(\varepsilon_0+s\omega)t}\end{aligned} \tag{2.25}$$

Eqn. (2.25) means the states of two energies ε_1 and ε_2 are decoupled if $(\varepsilon_1-\varepsilon_2)/\omega\notin\mathbb{Z}$. Therefore the summation over ε_0 can be omitted in Eqn. (2.25):

$$\sum_{s}\left(\delta_{s,0}+R_s\right)e^{-i\varepsilon_s t}=\sum_{m,s}\left(A_m+B_m\right)J_{s-m}(\tfrac{V_0}{\omega})e^{-i\varepsilon_s t} \tag{2.26 a}$$

, with a short-hand notations that $\varepsilon_m\equiv\varepsilon_0+m\omega$, $R_s\equiv R_{\varepsilon_0+s\omega}$, etc. The coefficients $c^{(I)}_{p_{\varepsilon_0+s\omega}}$ are also replaced by $\delta_{s,0}$ without losing any generality. Therefore, the incident wave is a single state with a definite energy ε_0 and unity amplitude.

Eqn. (2.26 a) contains a set of linear equations. The other sets of equations form the rest boundary conditions are list below without derivations:

$$\sum_{s}\left(\delta_{s,0}e^{-ip_0 a}+R_s e^{-iq_s a}\right)e^{-i\varepsilon_s t}=\sum_{m,s}\left(A_m e^{-ip_m a}+B_m e^{-iq_m a}\right)J_{s-m}(\tfrac{V_0}{\omega})e^{-i\varepsilon_s t} \tag{2.26 b}$$

$$\sum_{m,s}\left(A_m e^{ip_m La}+B_m e^{iq_m La}\right)J_{s-m}(\tfrac{V_0}{\omega})e^{-i\varepsilon_s t}=\sum_{s}T_s e^{ip_s La}e^{-i\varepsilon_s t} \tag{2.26 c}$$

$$\sum_{m,s}\left(A_m e^{ip_m (L+1)a}+B_m e^{iq_m (L+1)a}\right)J_{s-m}(\tfrac{V_0}{\omega})e^{-i\varepsilon_s t}=\sum_{s}T_s e^{ip_s (L+1)a}e^{-i\varepsilon_s t} \tag{2.26 d}$$

The discussion above concludes that for the presence of time-dependent potential, the incident wave with a definite energy, ε_0, will be scattering into those states with energies $E=\varepsilon_s\equiv\varepsilon_0+s\omega$. The energy, ε_s, are referred to the *s-th sideband* (the 0-th sideband is denoted as the *central sideband*). The sideband structures for scattering states is determined numerically by Eqns. (2.26) with a cut off, $|s|\le N_s$.

2-4 Transmission dip structures

In this section we have a brief introduction of the form of conductance and density of state in order to explain the transmission dip structures.

$$J_{in}=J_T+J_R \tag{2.28}$$

J_{in} J_T J_R is incident current, transmission current, reflection current, respectively.

By matching the boundary condition and getting the current in each region we can write the total transmission T by observing the current conservation.

$$T=\frac{J_T}{J_{in}} \tag{2.27}$$

Density of state can be written as

$$D(\varepsilon)=\frac{dN}{d\varepsilon}=\frac{L}{2\pi}\frac{-1}{2at_0\sin(ka)} \tag{2.28}$$

Eq (2.8) will go to infinity when ka is either zero or $n\pi$. According to **Fig. 2.2 we can observe when** ka is zero, the energy is at lower band bottom; when ka is $n\pi$ the energy is at higher band bottom. Since the density of state at band bottom is so large that we predict the conductance will dramatically drop while energy is at band bottom.

Fig. 2.3 present the dip structure by observing the total transmission varies from incident energy. This is because the incident particle exchanges energy with the time-dependent potential. After emitting a photon with energy $\hbar\omega$ the energy is trapped at the band bottom which has large density of state, as a result the transmission dip appears. This result inspires us to discover the same physical

concept in Graphene.

In case of mistakes may happen, we introduce a way to check the inaccuracy σ_J by testing the current conservation. Where N is the amount of data, i label the region of current, see Fig 4.1. For instance, $N=100$ means we have 100 data and $i=2$ means the II region of current is considered.

$$\sigma_J = \sqrt{\frac{1}{3N}\sum_{j}^{N}\sum_{i}^{3}\left(J_{ij}-\bar{J}_j\right)^2} \tag{2.29}$$

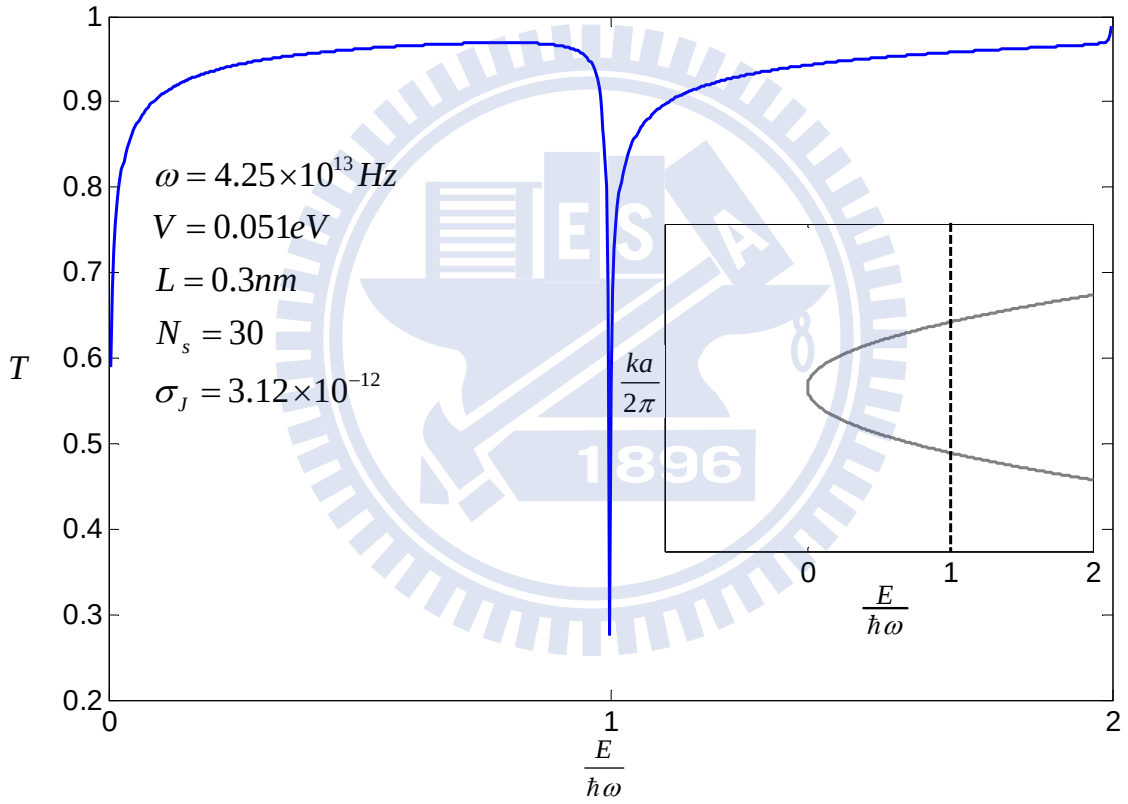

Fig. 2.4 Transmission dip structure appears when the first sideband reaches the band bottom(emit one photon with energy $\hbar\omega$). L refers to the width of barrier in unit of lattice constant. σ indicates the degree of inaccuracy.

Chapter 3

Theoretical basics in graphene

The theoretical basics in graphene are briefly presented in this chapter. In **Sec. 3-1**, the tight-binding model in graphene is discussed including band structure and the valley degrees of freedom. The 2D Dirac-like effective Hamiltonian of low energy excitations is in **Sec. 3-2**. In **Sec. 3-3**, the exotic phenomena related the chirality of electron called Klein tunneling is given.

3-1 Two dimensional tight-binding Hamiltonian in graphene

A graphene sheet shown in **Fig. 3.1** is a honeycomb structure composed by carbon atoms at every corner of hexagons. The structure can be seen as a triangular lattice with a basis of two carbons (A and B distinguished by ● and ○, respectively) per unit cell. The primitive lattice vectors $\left\{\boldsymbol{a}_1 = a_0\left(\frac{1}{2}\hat{x}+\frac{\sqrt{3}}{2}\hat{y}\right)=\boldsymbol{a}_x+\boldsymbol{a}_y, \boldsymbol{a}_2 = a_0\left(-\frac{1}{2}\hat{x}+\frac{\sqrt{3}}{2}\hat{y}\right)=-\boldsymbol{a}_x+\boldsymbol{a}_y\right\}$ are also exhibited with a_0 being the distance between two nearest carbons.

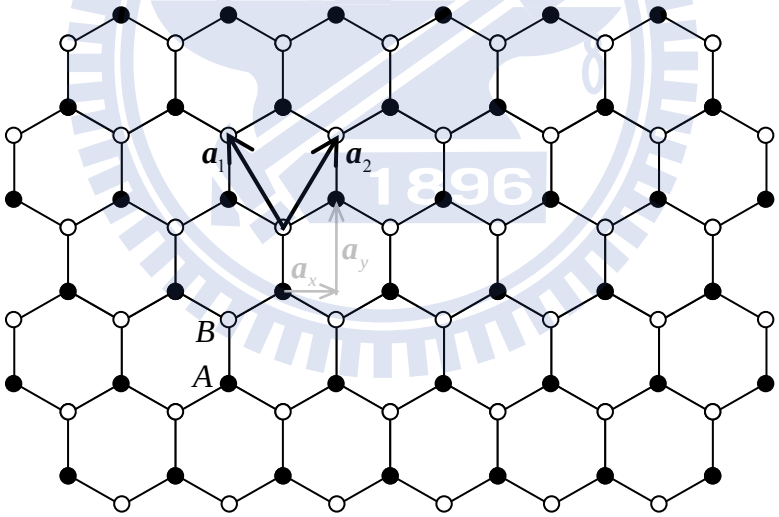

Fig. 3.1 the two dimensional graphene sheet. The honeycomb structure is composed by a triangular lattice with two carbon atoms (distinguished by A (●) and B(○)) on every lattice site. The conventional primitive lattice vectors, $\{\boldsymbol{a}_1, \boldsymbol{a}_2\}$, are denoted.

In reciprocal space, the primitive lattice vectors are $\left\{\boldsymbol{b}_1 = \frac{2\pi}{3a}\left(\sqrt{3}\hat{x}+\hat{y}\right),\ \boldsymbol{b}_2 = \frac{2\pi}{3a}\left(-\sqrt{3}\hat{x}+\hat{y}\right)\right\}$.

The Brillouin zone of a triangular lattice is a hexagon as shown in **Fig. 3.2**. The six corners (***K*** points) of the hexagon are coupled by $\{\boldsymbol{b}_1, \boldsymbol{b}_2\}$, and separated into two distinct groups, $\boldsymbol{K}_1$ and $\boldsymbol{K}_2$ (in **Fig. 3.2**). These two points can be identified by the valley-shaped from dispersion (**Fig. 3.3**). In graphene, there are plenty of physics related to the two valleys and these will be introduced in the following

sections in this chapter.

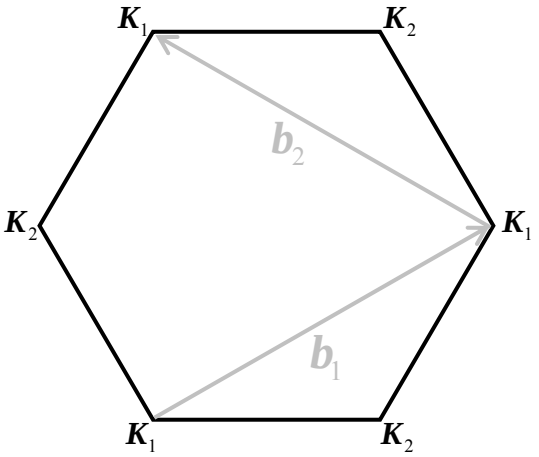

Fig. 3.2 the Brillouin zone. The six ***K***-points are categorized into two groups: $\boldsymbol{K}_1 = K\hat{x} = \frac{4\pi}{3\sqrt{3}a}(1,0)$ and $\boldsymbol{K}_2 = -K\hat{x} = \frac{4\pi}{3\sqrt{3}a}(-1,0)$.

The basic dispersion feature of graphene can be characterized by the 1st nearest neighbor tight-binding model:

$$\hat{H} = -t_0 \sum_{m,n} \begin{bmatrix} \left(|m,n;B\rangle + |m-1,n;B\rangle + |m,n-1;B\rangle\right)\langle m,n;A| + \\ \left(|m,n;A\rangle + |m+1,n;A\rangle + |m,n+1;A\rangle\right)\langle m,n;B| \end{bmatrix} \tag{3.1}$$

The eigen-basis of Eqn. (3.1) is in Bloch type:

$$|\boldsymbol{k}\rangle = \sum_{m,n} e^{i\boldsymbol{k}\cdot\boldsymbol{R}_{mn}} \left\{ C_A |m,n;A\rangle + C_B |m,n;B\rangle \right\} \tag{3.2}$$

By Eqns. (3.1) and (3.2), the eigenvalue equation, $\hat{H}|\boldsymbol{k}\rangle = E|\boldsymbol{k}\rangle$, can be casted into

$$\begin{bmatrix} 0 & h_{\boldsymbol{k}} \\ \tilde{h}_{\boldsymbol{k}} & 0 \end{bmatrix} \begin{bmatrix} C_A \\ C_B \end{bmatrix} = E \begin{bmatrix} C_A \\ C_B \end{bmatrix}, \tag{3.3}$$

with

$$h_{\boldsymbol{k}} = -t_0 \left(1 + e^{-i\boldsymbol{k}\cdot\boldsymbol{a}_1} + e^{-i\boldsymbol{k}\cdot\boldsymbol{a}_2}\right) = -t_0 \left(1 + 2e^{-ik_y a_y} \cos\left(k_x a_x\right)\right), \text{ and}$$
$$\tilde{h}_{\boldsymbol{k}} = -t_0 \left(1 + e^{i\boldsymbol{k}\cdot\boldsymbol{a}_1} + e^{i\boldsymbol{k}\cdot\boldsymbol{a}_2}\right) = -t_0 \left(1 + 2e^{ik_y a_y} \cos\left(k_x a_x\right)\right).$$

From Eqn. (3.3), the energy dispersion has an analytical form:

$$E(\boldsymbol{k}) = \pm\sqrt{h_{\boldsymbol{k}}\tilde{h}_{\boldsymbol{k}}} = \pm t_0 \sqrt{1 + 4\cos\left(k_y a_y\right)\cos\left(k_x a_x\right) + 4\cos^2\left(k_x a_x\right)} \tag{3.4}$$

Solutions of Eqn. (3.3) reveal the Bloch electrons in graphene are related to two-component columns named pseudo-spin,

$$\chi_{\boldsymbol{k}} = \begin{pmatrix} C_A(\boldsymbol{k}) \\ C_B(\boldsymbol{k}) \end{pmatrix}. \tag{3.5}$$

In low energy limit, the pseudo-spin is modeled by the 2D Dirac electron's chiralty. The details are presented in next section.

If there is an onsite energy difference, 2Δ, between A and B atoms, a gap is introduced. Thus, the Hamiltonian in Eqn. (3.1) is modified as:

$$\hat{H} = -t_0 \sum_{m,n} \begin{bmatrix} \left(|m,n;B\rangle + |m-1,n;B\rangle + |m,n-1;B\rangle\right)\langle m,n;A| + \\ \left(|m,n;A\rangle + |m+1,n;A\rangle + |m,n+1;A\rangle\right)\langle m,n;B| \end{bmatrix} + \Delta \sum_{m,n} \begin{bmatrix} |m,n;A\rangle\langle m,n;A| - \\ |m,n;B\rangle\langle m,n;B| \end{bmatrix} \tag{3.6}$$

Eqns. (3.3) and (3.4) are also replaced accordingly:

$$\begin{bmatrix} \Delta & h_{\mathbf{k}} \\ \tilde{h}_{\mathbf{k}} & -\Delta \end{bmatrix} \begin{bmatrix} C_A \\ C_B \end{bmatrix} = E \begin{bmatrix} C_A \\ C_B \end{bmatrix} \tag{3.7}$$

$$E(\boldsymbol{k}) = \pm\sqrt{\Delta^2 + h_{\mathbf{k}}\tilde{h}_{\mathbf{k}}} = \pm t_0\sqrt{\Delta^2 + 1 + 4\cos\left(k_y a_y\right)\cos\left(k_x a_x\right) + 4\cos^2\left(k_x a_x\right)} \tag{3.8}$$

Fig. 3.3 shows the linear dispersions of gapless graphene at six K points. The dispersions for gapless/gapped graphene near six ***K*** points are modeled by the effective Hamiltonians, which are identical to those of the two-dimensional massless/massive Dirac fermions. **Fig. 3.4** displays these relativistic dispersions. The effective Hamiltonians is discussed in next section.

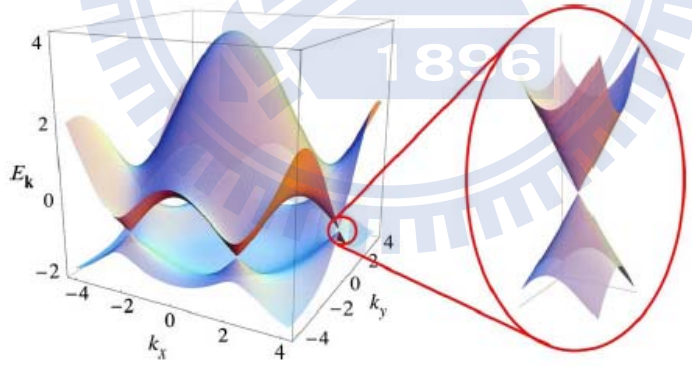

Fig. 3.3 Left :Dispersion energy spectrum in Graphene. Right : zoom in one of Dirac cones. Cite from The electron properties of Graphene (2009)

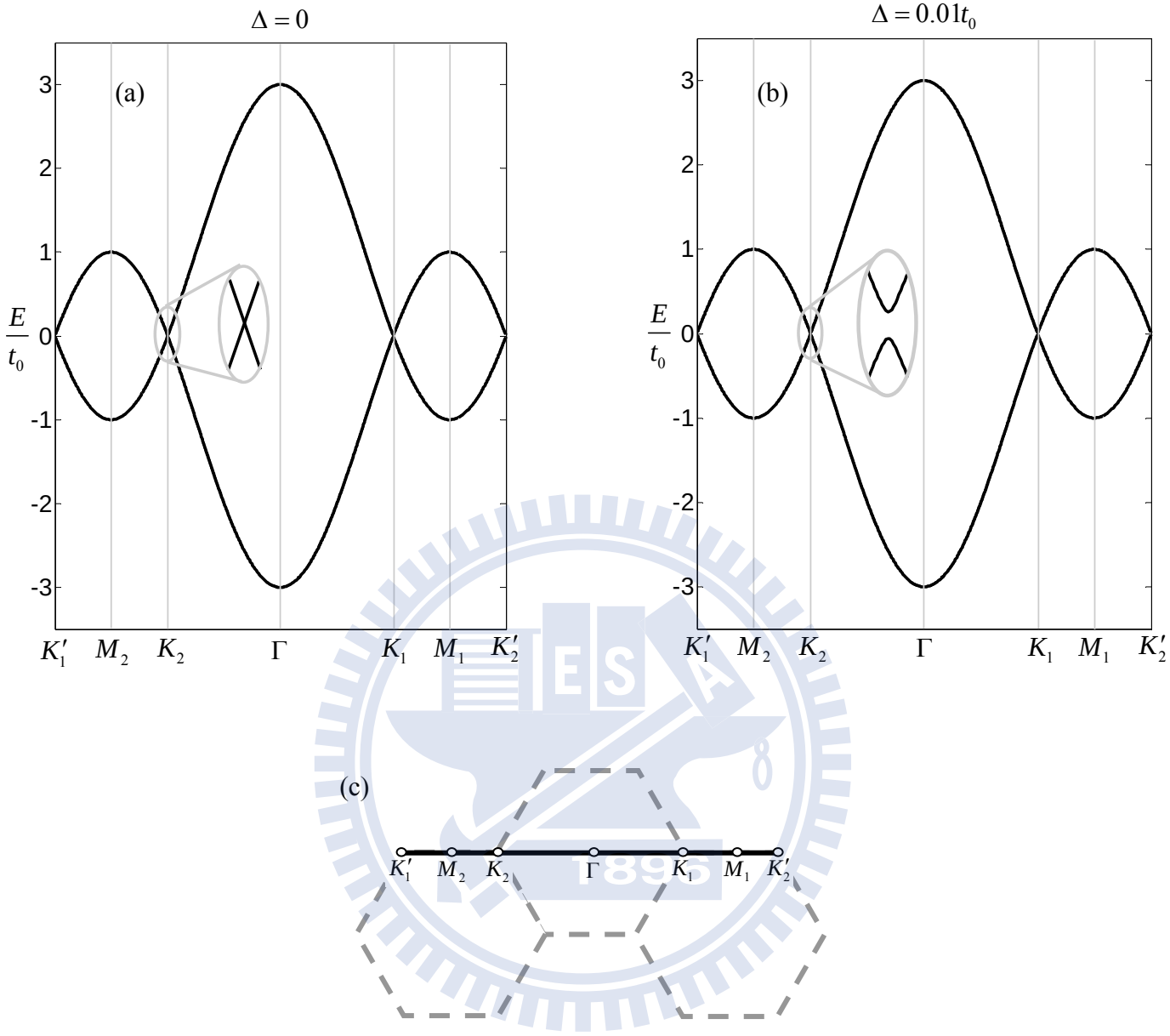

Fig. 3.4 dispersion relation of gapless/gapped graphene along $k_x = 0$. (a) gapless graphene, (b) gapped graphene, and (c) the related symmetry points in the Brillouin zone.

3-2 Effective Hamiltonian for low energy excitations

The effective Hamiltonian can be derived from small-$\boldsymbol{q}$ expansion at $\boldsymbol{K}_1$ and $\boldsymbol{K}_2$:

$$\begin{aligned} h_{\boldsymbol{k}=\tau K\hat{x}+\boldsymbol{q}} &\simeq \frac{3at_0}{2}\left(\tau q_x - iq_y\right) = v_F\left(\tau q_x - iq_y\right) \\ \tilde{h}_{\boldsymbol{k}=\tau K\hat{x}+\boldsymbol{q}} &\simeq \frac{3at_0}{2}\left(\tau q_x + iq_y\right) = v_F\left(\tau q_x + iq_y\right) \end{aligned} \tag{3.9}$$

; a valley-index, τ, is introduced to indicate $\boldsymbol{K}_1(\tau=+1)$ or $\boldsymbol{K}_2(\tau=-1)$ valleys. Therefore, from Eqns. (3.3) and (3.7) the effective Hamiltonians are:

$$\hat{H}_{eff} = v_F\begin{bmatrix} 0 & \tau q_x - iq_y \\ \tau q_x + iq_y & 0 \end{bmatrix} \tag{3.10}$$

, for gapless graphene while

$$\hat{H}_{eff} = \begin{bmatrix} \Delta & v_F\left(\tau q_x - iq_y\right) \\ v_F\left(\tau q_x + iq_y\right) & -\Delta \end{bmatrix} \tag{3.11}$$

, for gapped graphene. The dispersion of Eqns. (3.10) and (3.11) are $E_{\boldsymbol{q}} = \pm v_F|\boldsymbol{q}|$, and $E_{\boldsymbol{q}} = \pm\sqrt{v_F^2 q^2 + \Delta^2}$, respectively. Compare with the massless/massive relativistic dispersions, $E_{\boldsymbol{k}} = \pm c|\boldsymbol{k}|$, and $E_{\boldsymbol{k}} = \pm\sqrt{c^2k^2 + m_0^2c^4}$, the electrons in graphene with $E \ll t_0$ behave as relativistic fermions with the replacements: $c \to v_F$ and $m_0 \to \Delta / v_F^2$.

3-3 Klein tunneling:

When incident angle is zero, qusiparticles in graphene act like relativistic particles, Dirac fermions. At this incident angle, particle can make perfect transmission resulting from Chiral nature through a barrier no matter how high or wide it is. This exotic phenomenon is called Klein tunneling.

To prove that, we can substitute $k_y = 0$ into Eqn. (3.3) then we have

$$\begin{bmatrix} 0 & h_{\boldsymbol{k}} \\ h_{\boldsymbol{k}} & 0 \end{bmatrix}\begin{bmatrix} C_A \\ C_B \end{bmatrix} = E\begin{bmatrix} C_A \\ C_B \end{bmatrix} \tag{3.6}$$

Where the eigenvalues of Eqn. (3.5) are $E = \pm h_{\mathbf{k}}{}^2$. The two eigenvalues are shown in **Fig 3.5**, red and blue curve refer to $h_{\mathbf{k}}$ and $-h_{\mathbf{k}}$, respectively. These two eigenvectors will be orthogonal to each

other; hence the incident wave and reflection wave cannot propagate in the same valley. Since we have already known it is impossible to have transmission and reflection wave in the same valley, so we have the following question. Is there any possible to propagate from the other valley? Here since the incident energy we select is so close to Fermi energy that the reflection wave is very hard to propagate from the other valley due to large momentum transform. Hence the orthogonal property of eigenvectors and large momentum transform leads the transport to a perfect tunneling.

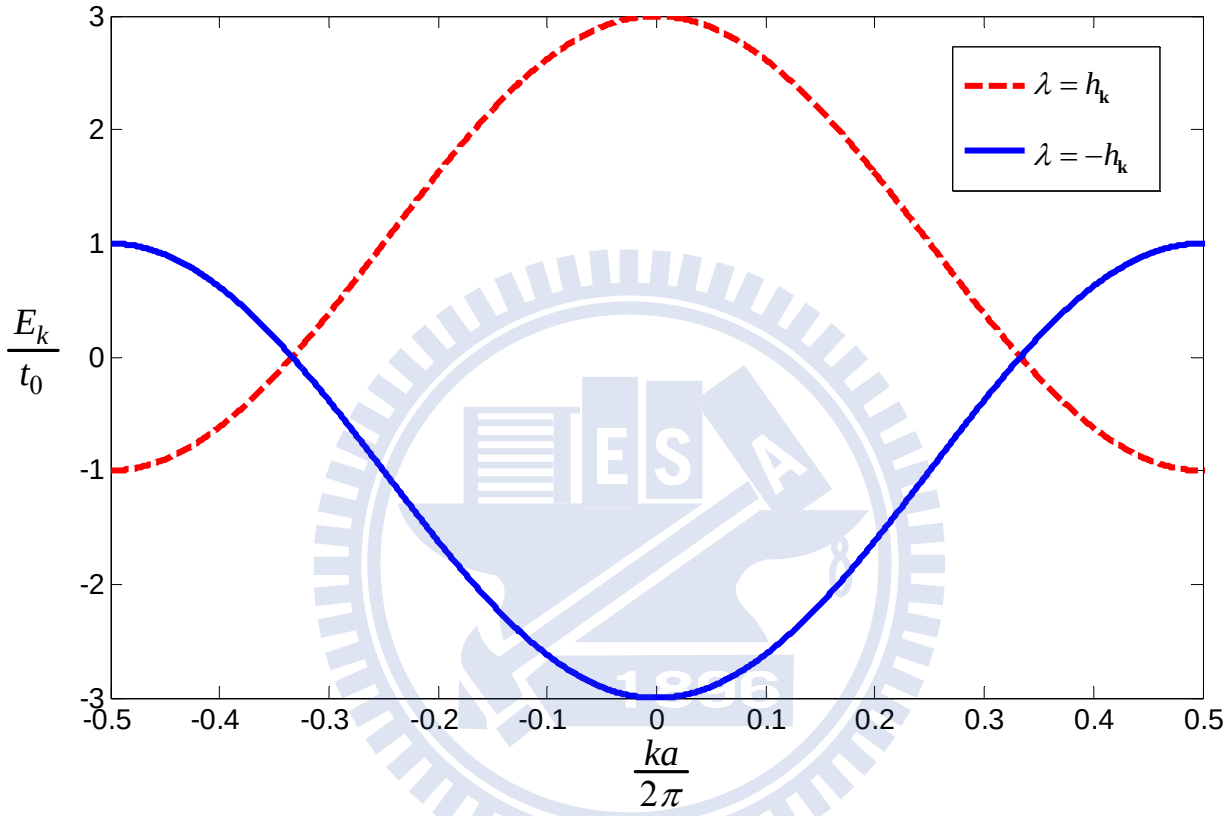

Fig. 3.5 Dispersion relation with normal incident particle. Red and blue curve refer to h_k and $-h_k$, respectively. K_1 valley is close to the cross point of these two curves at right hand side, the other cross point is labeled by K_2 valley.

Chapter 4

Time-dependent potential barrier in graphene

In this chapter, the time-dependent transport theory in graphene is exhibited. The system we interesting in is presented in **Sec. 4-1**. For the translational invariant along y-direction, the 2D tight-binding Hamiltonian is reduced into an 1D Schrodinger equation. Based on this 1D equation, the current and continuity equation is discussed in **Sec. 4-2**. To solve the scattering states with the presence of time-dependent potential barrier, the boundary conditions are derived in **Sec. 4-3**.

4-1 One-dimensional Schrödinger equation for graphene

The system with time-dependent potential is demonstrated in **Fig. 4.1**. A graphene sheet is divided into three regions for the presence of a potential barrier. The barrier is applied along the armchair orientation hence both intra- and inter-valley scattering are allowed in transport. **Fig. 4.1** also displays the conventional primitive lattice vectors, $\boldsymbol{a}_1 = (-\frac{1}{2}\hat{x} + \frac{\sqrt{3}}{2}\hat{y})a_0$ and $\boldsymbol{a}_2 = (\frac{1}{2}\hat{x} + \frac{\sqrt{3}}{2}\hat{y})a_0$, where a_0 is the distance between two nearest carbon atoms. Therefore, any lattice vector is expressed by $\boldsymbol{R}_{mn} = m\boldsymbol{a}_1 + n\boldsymbol{a}_2$. However, due to the translational invariance along y-direction, another more convenient lattice basis set is introduced:

$$\boldsymbol{R}_{mn} = m\boldsymbol{a}_1 + n\boldsymbol{a}_2 = (n-m)\frac{a_0}{2}\hat{x} + (n+m)\frac{\sqrt{3}a_0}{2}\hat{y} = M\boldsymbol{a}_x + N\boldsymbol{a}_y \tag{4.1}$$

with $\boldsymbol{a}_x = \frac{a_0}{2}\hat{x}$ and $\boldsymbol{a}_y = \frac{\sqrt{3}a_0}{2}\hat{y}$; $(M,N) = (n-m, n+m)$. Within this *M*-*N* coordinate, the three regions (Region I, II, and III) are characterized by $M < 0$, $0 \le M \le L$, and $M > L$, respectively (**Fig. 4.1**). In the following, this new basis set is employed to derive the one-dimensional (1D) Schrödinger equation in graphene.

The Hamiltonian of this system is

$$\begin{aligned}
&\hat{H}_0 + \hat{V}(t) \\
&= -t_0 \sum_{M,N} \left[\begin{array}{l} \left(|M-1, N+1; A\rangle + |M+1, N+1; A\rangle + |M, N; A\rangle \right) \langle M, N; B| + \\ \left(|M+1, N-1; B\rangle + |M-1, N-1; B\rangle + |M, N; B\rangle \right) \langle M, N; A| \end{array} \right] + \\
&\sum_{M,N} \left\{ V(M)\cos(\omega t) \left(\begin{array}{l} |M, N; A\rangle\langle M, N; A| + \\ |M, N; B\rangle\langle M, N; B| \end{array} \right) + \Delta \left(\begin{array}{l} |M, N; A\rangle\langle M, N; A| - \\ |M, N; B\rangle\langle M, N; B| \end{array} \right) \right\}
\end{aligned} \tag{4.2}$$

where 2Δ defines the size of gap and the amplitude of the time-dependent barrier has the spatial form:

$$V(M)=\begin{cases}0 & M<0 \text{ or } M>L\\ V_0 & 0\le M\le L\end{cases}.$$

Since the translational invariance along y, the wave function is characterized by a single k_y, and written as

$$\begin{aligned}\psi &= \sum_{M,N}\left(\widetilde{f_A}(M,N;t)\left|M,N;A\right\rangle+\widetilde{f_B}(M,N;t)\left|M,N;B\right\rangle\right)\\ &= \sum_{M,N} e^{iNk_y a_y}\left(f_{A,k_y}(M;t)\left|M,N;A\right\rangle+f_{B,k_y}(M;t)\left|M,N;B\right\rangle\right).\end{aligned} \tag{4.3}$$

For abbreviated notation, $f_{\eta,k_y}(M;t)\equiv f_\eta(M;t)$ for $\eta = A$ or B.

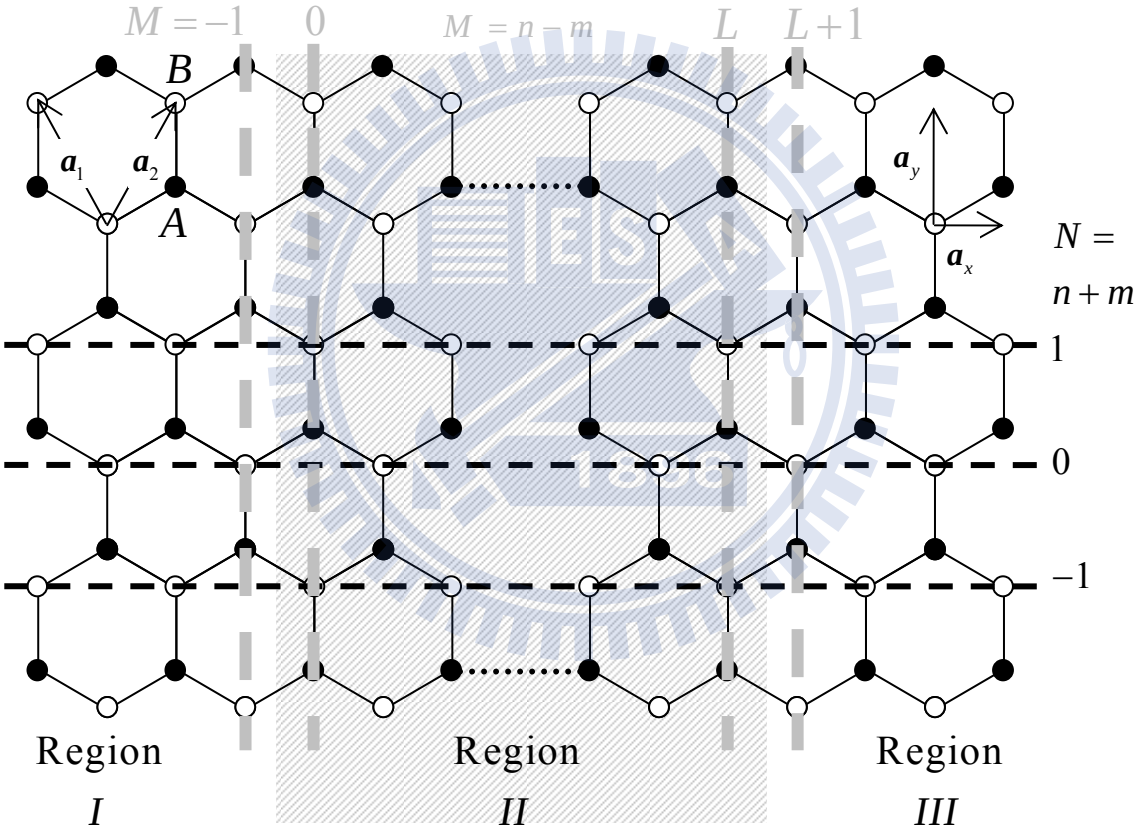

Fig. 4.1. The graphene sheet is divided into three regions. In region II ($0\le M\le L$), a time-dependent potential, $V(t)=V_0\cos(\omega t)$ is presented. The sublattices A and B are denoted as ○ and ●, respectively. The conventional primitive lattice vectors, $\{\boldsymbol{a}_1,\boldsymbol{a}_2\}$, and x-y lattice vectors, $\{\boldsymbol{a}_x,\boldsymbol{a}_y\}$, are labeled. Each lattice site can be represented by $m\boldsymbol{a}_1+n\boldsymbol{a}_2=(n-m)\boldsymbol{a}_x+(n+m)\boldsymbol{a}_y=M\boldsymbol{a}_x+N\boldsymbol{a}_y$.

Combination of Eqns. (4.2) and (4.3) results in

$$
\begin{aligned}
&-t_0 \sum_{M,N} e^{iNk_y a_y} \begin{bmatrix} f_B(M;t)\left(\left|M-1,N+1;A\right\rangle+\left|M+1,N+1;A\right\rangle+\left|M,N;A\right\rangle\right)+ \\ f_A(M;t)\left(\left|M+1,N-1;B\right\rangle+\left|M-1,N-1;B\right\rangle+\left|M,N;B\right\rangle\right) \end{bmatrix} \\
&+\sum_{M,N}\left\{V_0\cos(\omega t)e^{iNk_y a_y}\begin{pmatrix} f_A(M;t)\left|M,N;A\right\rangle+ \\ f_B(M;t)\left|M,N;B\right\rangle \end{pmatrix}+\Delta e^{iNk_y a_y}\begin{pmatrix} f_A(M;t)\left|M,N;A\right\rangle- \\ f_B(M;t)\left|M,N;B\right\rangle \end{pmatrix}\right\} \qquad (4.4) \\
&=i\sum_{M,N}\partial_t\left(f_A(M;t)\left|M,N;A\right\rangle+f_B(M;t)\left|M,N;B\right\rangle\right)e^{iNk_y a_y} \qquad (\hbar=1)
\end{aligned}
$$

Inner product Eqn. (4.4) with $\langle M,N;\eta|$, we have

$$
\begin{aligned}
&-t_0\left[\left(f_B(M+1;t)+f_B(M-1;t)\right)e^{-ik_y a_y}+f_B(M;t)\right] \\
&\qquad\qquad +\left\{V(M)\cos(\omega t)+\Delta\right\}f_A(M;t)=i\partial_t f_A(M;t) \\
&-t_0\left[\left(f_A(M-1;t)+f_A(M+1;t)\right)e^{ik_y a_y}+f_A(M;t)\right] \\
&\qquad\qquad +\left\{V(M)\cos(\omega t)-\Delta\right\}f_B(M;t)=i\partial_t f_B(M;t)
\end{aligned} \qquad (4.5)
$$

By defining

$$
\hat{T}\equiv\begin{bmatrix} 0 & e^{-ik_y a_{1y}} \\ e^{ik_y a_{1y}} & 0 \end{bmatrix};\quad \boldsymbol{f}_M\equiv\begin{bmatrix} f_A(M;t) \\ f_B(M;t) \end{bmatrix},
$$

Eqn. (4.5) is rewritten as

$$
-t_0\left(\hat{T}\boldsymbol{f}_{M+1}+\hat{T}\boldsymbol{f}_{M-1}+\hat{\sigma}_x\boldsymbol{f}_M\right)+V(M)\cos(\omega t)\,\boldsymbol{f}_M+\Delta\sigma_z\boldsymbol{f}_M=i\partial_t\boldsymbol{f}_M \qquad (4.6)
$$

Eqn. (4.6) is the 1D Schrödinger equation for the system.

4-2 Current and continuity equation

From the Schrödinger equation, the probability density is defined as

$$
\rho(M;t)=\boldsymbol{f}_M^{\dagger}\boldsymbol{f}_M/a_x. \qquad (4.7)
$$

To derive the tight-binding version of continuity equation and the related current form, differentiate Eqn. (4.7) w.r.t. time and combine with Eqn. (4.6):

$$
\begin{aligned}
-\partial_t\rho&=-\frac{\left(\partial_t\boldsymbol{f}_M^{\dagger}\right)\boldsymbol{f}_M}{a_x}-\frac{\boldsymbol{f}_M^{\dagger}\left(\partial_t\boldsymbol{f}_M\right)}{a_x} \\
&=\frac{it_0}{a_x}\left(\boldsymbol{f}_{M+1}^{\dagger}\hat{T}\boldsymbol{f}_M+\boldsymbol{f}_{M-1}^{\dagger}\hat{T}\boldsymbol{f}_M\right)-\frac{it_0}{a_x}\left(\boldsymbol{f}_M^{\dagger}\hat{T}\boldsymbol{f}_{M+1}+\boldsymbol{f}_M^{\dagger}\hat{T}\boldsymbol{f}_{M-1}\right) \qquad (4.8\text{ a}) \\
&=\frac{it_0}{a_x}\left(\boldsymbol{f}_{M-1}^{\dagger}\hat{T}\boldsymbol{f}_M-\boldsymbol{f}_M^{\dagger}\hat{T}\boldsymbol{f}_{M-1}-\boldsymbol{f}_M^{\dagger}\hat{T}\boldsymbol{f}_{M+1}+\boldsymbol{f}_{M+1}^{\dagger}\hat{T}\boldsymbol{f}_M\right)
\end{aligned}
$$

$$\Delta_M(j) \equiv \frac{it_0}{a_x}\left(\underbrace{\boldsymbol{f}_{M-1}^{\dagger}\hat{T}\boldsymbol{f}_M}_{\leftarrow} - \underbrace{\boldsymbol{f}_M^{\dagger}\hat{T}\boldsymbol{f}_{M-1}}_{\rightarrow} - \underbrace{\boldsymbol{f}_M^{\dagger}\hat{T}\boldsymbol{f}_{M+1}}_{\leftarrow} + \underbrace{\boldsymbol{f}_{M+1}^{\dagger}\hat{T}\boldsymbol{f}_M}_{\rightarrow} \right) \tag{4.8 b}$$

Eqn. (4.8 b) defines form of $\nabla \cdot \boldsymbol{j}$ for the 1D Schrödinger equation. There is an arrow below each term in Eqn. (4.8 b) indicating the direction of particle flux. These arrows reveal $\Delta_M(j)$ is proportional to outgoing flux. This engages us to conjecture the form of current, which is proportional to right-going flux:

$$j_M \propto \overbrace{\boldsymbol{f}_M^{\dagger}\hat{T}\boldsymbol{f}_{M-1}}^{\rightarrow} - \overbrace{\boldsymbol{f}_{M-1}^{\dagger}\hat{T}\boldsymbol{f}_M}^{\leftarrow} + \overbrace{\boldsymbol{f}_{M+1}^{\dagger}\hat{T}\boldsymbol{f}_M}^{\rightarrow} - \overbrace{\boldsymbol{f}_M^{\dagger}\hat{T}\boldsymbol{f}_{M+1}}^{\leftarrow}$$

To investigate this conjecture, $\Delta_M(j)$ is examined in the long wavelength limit. In this limit, the wave function, $\boldsymbol{f}_{M\pm1}$, is expanded as

$$\boldsymbol{f}_{M\pm1} = \boldsymbol{f}(Ma_x \pm a_x) \simeq \boldsymbol{f}_M \pm a_x(\partial_x \boldsymbol{f})_M + \frac{a_x^2}{2}(\partial_x^2 \boldsymbol{f})_M \tag{4.9}$$

Therefore,

$$\Delta_M(j) \simeq -it_0 a_x \partial_x \left[\boldsymbol{f}_M^{\dagger}\hat{T}(\partial_x \boldsymbol{f})_M - (\partial_x \boldsymbol{f}^{\dagger})_M \hat{T}\boldsymbol{f}_M \right] \tag{4.10}$$

Eqn. (4.10) demonstrates the current form in the long wavelength limit:

$$\begin{aligned} j_M &= it_0 a_x \left[(\partial_x \boldsymbol{f}^{\dagger})_M \hat{T}\boldsymbol{f}_M - \boldsymbol{f}_M^{\dagger}\hat{T}(\partial_x \boldsymbol{f})_M \right] \\ &= \frac{it_0}{2}\left[(\boldsymbol{f}_{M+1}^{\dagger} - \boldsymbol{f}_{M-1}^{\dagger})\hat{T}\boldsymbol{f}_M - \boldsymbol{f}_M^{\dagger}\hat{T}(\boldsymbol{f}_{M+1} - \boldsymbol{f}_{M-1}) \right] \end{aligned} \tag{4.11}$$

Eqn. (4.11) confirms the conjecture from Eqn. (4.8).

The time average current is spatially independent. To show this, $j_M - j_{M-1}$ is calculated:

$$\begin{aligned} j_M - j_{M-1} &= \frac{it_0}{2}\left\{ \begin{array}{l} \left[(\boldsymbol{f}_{M+1}^{\dagger} - \boldsymbol{f}_{M-1}^{\dagger})\hat{T}\boldsymbol{f}_M - \boldsymbol{f}_M^{\dagger}\hat{T}(\boldsymbol{f}_{M+1} - \boldsymbol{f}_{M-1}) \right] - \\ \left[(\boldsymbol{f}_M^{\dagger} - \boldsymbol{f}_{M-2}^{\dagger})\hat{T}\boldsymbol{f}_{M-1} - \boldsymbol{f}_{M-1}^{\dagger}\hat{T}(\boldsymbol{f}_M - \boldsymbol{f}_{M-2}) \right] \end{array} \right\} \\ &= \frac{it_0}{2}\left(\boldsymbol{f}_{M+1}^{\dagger}\hat{T}\boldsymbol{f}_M - \boldsymbol{f}_M^{\dagger}\hat{T}\boldsymbol{f}_{M+1} + \boldsymbol{f}_{M-2}^{\dagger}\hat{T}\boldsymbol{f}_{M-1} - \boldsymbol{f}_{M-1}^{\dagger}\hat{T}\boldsymbol{f}_{M-2} \right) \\ &= \frac{it_0}{2}\left\{ \begin{array}{l} \left(\cancel{\boldsymbol{f}_{M-1}^{\dagger}\hat{T}\boldsymbol{f}_M} - \cancel{\boldsymbol{f}_M^{\dagger}\hat{T}\boldsymbol{f}_{M-1}} - \boldsymbol{f}_M^{\dagger}\hat{T}\boldsymbol{f}_{M+1} + \boldsymbol{f}_{M+1}^{\dagger}\hat{T}\boldsymbol{f}_M \right) + \\ \left(\boldsymbol{f}_{M-2}^{\dagger}\hat{T}\boldsymbol{f}_{M-1} - \boldsymbol{f}_{M-1}^{\dagger}\hat{T}\boldsymbol{f}_{M-2} - \cancel{\boldsymbol{f}_{M-1}^{\dagger}\hat{T}\boldsymbol{f}_M} + \cancel{\boldsymbol{f}_M^{\dagger}\hat{T}\boldsymbol{f}_{M-1}} \right) \end{array} \right\} \\ &= \frac{1}{2}\left(\Delta_M(j) + \Delta_{M-1}(j) \right) \end{aligned}$$

Because $\boldsymbol{f}_M(t) = \sum_{\omega} \tilde{\boldsymbol{f}}_M(\omega) e^{-i\omega t}$, the time average of $\Delta_M(j)$ is

$$\left\langle \Delta_M(j) \right\rangle_t = \left\langle -\partial_t \rho(M) \right\rangle_t = -\left\langle \partial_t \left(\boldsymbol{f}_M^\dagger \boldsymbol{f}_M \right)/a_x \right\rangle_t$$
$$= \frac{i}{a_x} \left\langle \sum_{\omega,\omega'} (\omega-\omega') \tilde{\boldsymbol{f}}_M^\dagger(\omega') \tilde{\boldsymbol{f}}_M(\omega) e^{-i(\omega-\omega')t} \right\rangle_t = 0$$

Hence, $\langle j_M \rangle_t - \langle j_{M-1} \rangle_t = 0$; i.e. the time average current is spatially independent.

4-3 Boundary conditions and scattering states

The 1D Schrödinger equation implies the boundary conditions between the three regions. To derive these conditions, the Schrödinger equation (Eqn. (4.6)) is divided into three equations:

$$-t_0\left(\hat{T}\boldsymbol{f}_{M+1} + \hat{T}\boldsymbol{f}_{M-1} + \hat{\sigma}_x \boldsymbol{f}_M\right) + \Delta\sigma_z \boldsymbol{f}_M = i\partial_t \boldsymbol{f}_M \qquad M \le -1 \qquad (4.12\text{ a})$$

$$\left\{\begin{matrix} -t_0\left(\hat{T}\boldsymbol{f}_{M+1} + \hat{T}\boldsymbol{f}_{M-1} + \hat{\sigma}_x \boldsymbol{f}_M\right) + \\ V_0\cos(\omega t)\,\boldsymbol{f}_M + \Delta\sigma_z \boldsymbol{f}_M \end{matrix}\right\} = i\partial_t \boldsymbol{f}_M \qquad 0 \le M \le L \qquad (4.12\text{ b})$$

$$-t_0\left(\hat{T}\boldsymbol{f}_{M+1} + \hat{T}\boldsymbol{f}_{M-1} + \hat{\sigma}_x \boldsymbol{f}_M\right) + \Delta\sigma_z \boldsymbol{f}_M = i\partial_t \boldsymbol{f}_M \qquad M \ge L+1 \qquad (4.12\text{ c})$$

Note the constraints imposed in each equation in Eqn. (4.12). For example, Eqn. (4.12 a) holds only for those $M \le -1$. To derive the boundary conditions, ***the auxiliary functions***, $\boldsymbol{F}_M^{(I)}, \boldsymbol{F}_M^{(II)}$, and $\boldsymbol{F}_M^{(III)}$ are introduced by the following Schrödinger equations without any spatial constraint:

$$-t_0\left(\hat{T}\boldsymbol{F}_{M+1}^{(I)} + \hat{T}\boldsymbol{F}_{M-1}^{(I)} + \hat{\sigma}_x \boldsymbol{F}_M^{(I)}\right) + \Delta\sigma_z \boldsymbol{F}_M^{(I)} = i\partial_t \boldsymbol{F}_M^{(I)} \qquad (4.13\text{ a})$$

$$\left\{\begin{matrix} -t_0\left(\hat{T}\boldsymbol{F}_{M+1}^{(II)} + \hat{T}\boldsymbol{F}_{M-1}^{(II)} + \hat{\sigma}_x \boldsymbol{F}_M^{(II)}\right) + \\ V_0\cos(\omega t)\,\boldsymbol{F}_M^{(II)} + \Delta\sigma_z \boldsymbol{F}_M^{(II)} \end{matrix}\right\} = i\partial_t \boldsymbol{F}_M^{(II)} \qquad (4.13\text{ b})$$

$$-t_0\left(\hat{T}\boldsymbol{F}_{M+1}^{(III)} + \hat{T}\boldsymbol{F}_{M-1}^{(III)} + \hat{\sigma}_x \boldsymbol{F}_M^{(III)}\right) + \Delta\sigma_z \boldsymbol{F}_M^{(III)} = i\partial_t \boldsymbol{F}_M^{(III)} \qquad (4.13\text{ c})$$

By Eqns. (4.12) and (4.13), the auxiliary functions are further required that

$$\begin{aligned} \boldsymbol{F}_M^{(I)}(t) &= \boldsymbol{f}_M(t) && M \le -1 \\ \boldsymbol{F}_M^{(II)}(t) &= \boldsymbol{f}_M(t) && 0 \le M \le L \\ \boldsymbol{F}_M^{(III)}(t) &= \boldsymbol{f}_M(t) && L \le M \end{aligned} \qquad (4.14)$$

At boundary $M = -1$, Eqn. (4.12 a) read as:

$$-t_0\left(\hat{T}\boldsymbol{f}_0 + \hat{T}\boldsymbol{f}_{-2} + \hat{\sigma}_x \boldsymbol{f}_{-1}\right) + \Delta\sigma_z \boldsymbol{f}_{-1} = i\partial_t \boldsymbol{f}_{-1}, \qquad (4.15)$$

and from Eqn. (4.13 a):

$$-t_0\left(\hat{T}\boldsymbol{F}_0^{(I)} + \hat{T}\boldsymbol{F}_{-2}^{(I)} + \hat{\sigma}_x \boldsymbol{F}_{-1}^{(I)}\right) + \Delta\sigma_z \boldsymbol{F}_{-1}^{(I)} = i\partial_t \boldsymbol{F}_{-1}^{(I)} \qquad (4.16)$$

Combination of Eqns. (4.14), (4.15), and (4.16) leads to the boundary condition at $M = 0$:

$$\boldsymbol{F}_0^{(I)}(t) = \boldsymbol{f}_0(t) = \boldsymbol{F}_0^{(II)}(t) \tag{4.17 a}$$

Similar procedures will lead to other boundary conditions and they are listed below with derivations omitted:

$$\boldsymbol{F}_{-1}^{(II)}(t) = \boldsymbol{f}_{-1}(t) = \boldsymbol{F}_{-1}^{(I)}(t) \tag{4.17 b}$$

$$\boldsymbol{F}_L^{(III)}(t) = \boldsymbol{f}_L(t) = \boldsymbol{F}_L^{(II)}(t) \tag{4.17 c}$$

$$\boldsymbol{F}_{L+1}^{(II)}(t) = \boldsymbol{f}_{L+1}(t) = \boldsymbol{F}_{L+1}^{(III)}(t) \tag{4.17 d}$$

For the auxiliary functions and the boundary conditions between them, the *right-going scattering states*, $\boldsymbol{f}_M(t)$, is ready to be solved. As indicated in **Chapter 2**, the procedures are departed into two steps: write down the general forms of the auxiliary functions from the Schrodinger equations in Eqns. (4.13) individually, then impose the boundary conditions from Eqn. (4.17) that $\boldsymbol{f}_M(t)$ is the combination of $\boldsymbol{F}_M^{(I)}$, $\boldsymbol{F}_M^{(II)}$, and $\boldsymbol{F}_M^{(III)}$ in three regions.

At the first stage, the general forms of $\boldsymbol{F}_M^{(I)}$, $\boldsymbol{F}_M^{(II)}$, and $\boldsymbol{F}_M^{(III)}$ are inspired by Eqns. (2.4) and (2.5):

$$\begin{aligned}\boldsymbol{F}_M^{(I)}(t) &= \tfrac{1}{\sqrt{N}}\sum_{k_x} c_{k_x}^{(I)} e^{-iE(k_x)t} e^{ik_x Ma_x} \boldsymbol{\chi}_{k_x} \\ &= \tfrac{1}{\sqrt{N}}\sum_{\varepsilon,\tau}\left(c_{p_\varepsilon^{(\tau)}}^{(I)} e^{ip_\varepsilon^{(\tau)} Ma_x} \boldsymbol{\chi}_{p_\varepsilon^{(\tau)}} + R_\varepsilon^{(\tau)} e^{iq_\varepsilon^{(\tau)} Ma_x} \boldsymbol{\chi}_{q_\varepsilon^{(\tau)}} \right) e^{-i\varepsilon t}\end{aligned} \tag{4.18 a}$$

$$\begin{aligned}\boldsymbol{F}_M^{(II)}(t) &= \tfrac{1}{\sqrt{N}}\sum_{k_x,m} c_{k_x}^{(II)} J_m(\tfrac{V_0}{\omega}) e^{-i(E(k_x)+m\omega)t} e^{ik_x Ma_x} \boldsymbol{\chi}_{k_x} \\ &= \tfrac{1}{\sqrt{N}}\sum_{\varepsilon,\tau,m}\left(A_\varepsilon^{(\tau)} e^{ip_\varepsilon^{(\tau)} Ma_x} \boldsymbol{\chi}_{p_\varepsilon^{(\tau)}} + B_\varepsilon^{(\tau)} e^{iq_\varepsilon^{(\tau)} Ma_x} \boldsymbol{\chi}_{q_\varepsilon^{(\tau)}} \right) J_m(\tfrac{V_0}{\omega}) e^{-i(\varepsilon+m\omega)t}\end{aligned} \tag{4.18 b}$$

$$\boldsymbol{F}_M^{(III)}(t) = \tfrac{1}{\sqrt{N}}\sum_{k_x} c_{k_x}^{(III)} e^{-iE(k_x)t} e^{ik_x Ma_x} \boldsymbol{\chi}_{k_x} = \tfrac{1}{\sqrt{N}}\sum_{\varepsilon,\tau} T_\varepsilon^{(\tau)} e^{ip_\varepsilon^{(\tau)} Ma_x} e^{-i\varepsilon t} \boldsymbol{\chi}_{p_\varepsilon^{(\tau)}} \tag{4.18 c}$$

The pseudo-spin, $\boldsymbol{\chi}_{k_x}$, is introduced in **Chapter 3**. Note the summation over k_x in Eqns. (4.18) are transformed into summation over all possible energy, ε, and valley-index, τ (with $\tau = 1$ for K_1 and $\tau = 2$ for K_2). **Fig. 4.2** displays the dispersion relation, $E(k_x)$, with three typical values of k_y. For the valley structures, each valley, τ, contributes a right-going-*k*, $p_\varepsilon^{(\tau)}$, and a left-going-*k*, $q_\varepsilon^{(\tau)}$ for a given energy, ε. As mentioned in **Chapter 2**, the right/left-going-*k* are in the sense that the group velocities are right/left-going. **Fig. 4.3** illustrates the right-going scattering states constituted by these

$p_{\varepsilon}^{(\tau)}$ and $q_{\varepsilon}^{(\tau)}$. In **Appendix A**, the procedures to determine these Bloch wave vectors are discussed.

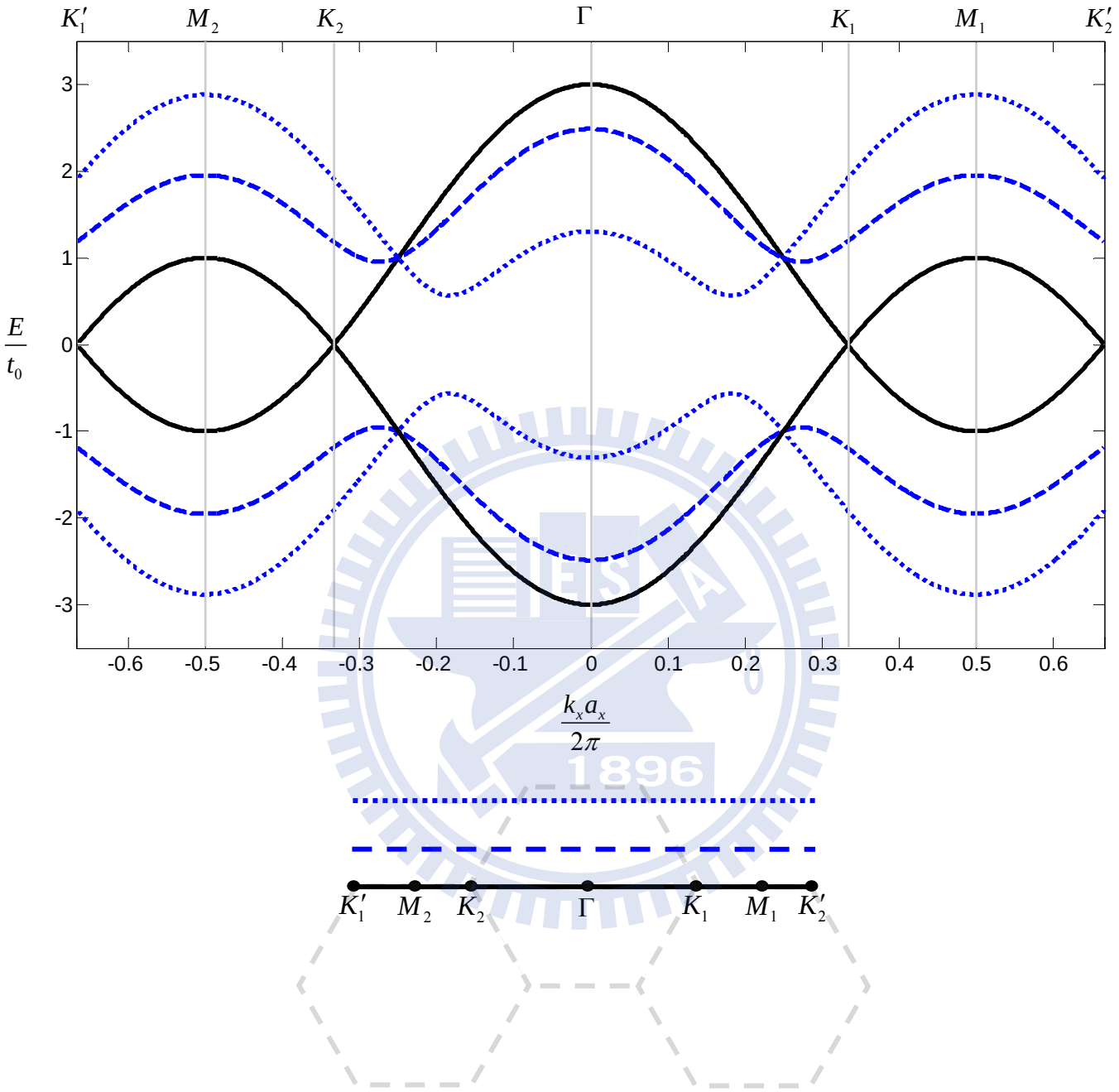

Fig. 4.2 dispersion relation with three typical values of k_y. M_1 and M_2 are the first Brillion zone boundaries in one dimensional momentum space of graphene.

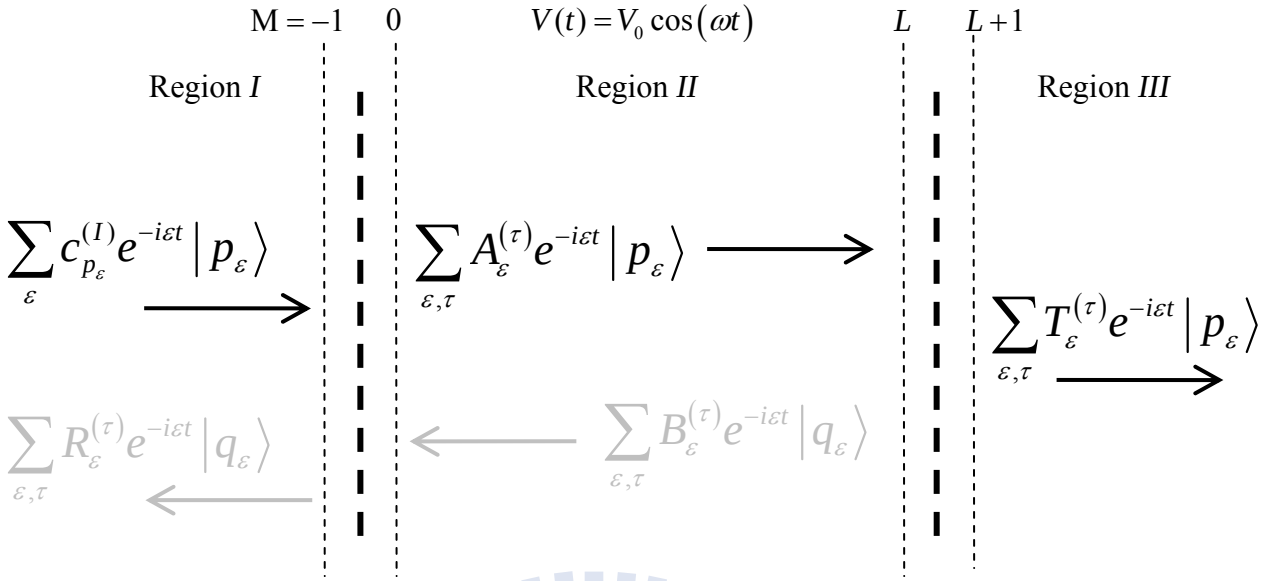

Fig. 4.3 The scattering states constituted by right/left-going states are also exhibited. The right-going states are shown with black color accompanied by black right arrows, while the left-going states are in gray color with gray left arrows.

For the 2nd stage, the boundary conditions require these auxiliary functions are equal for all time at the boundaries. For example, from Eqns. (4.17 a), (4.18 a) and (4.18 b) at $M = 0$:

$$\sum_{\varepsilon,\tau}\left(c^{(I)}_{p^{(\tau)}_{\varepsilon}}\boldsymbol{\chi}_{p^{(\tau)}_{\varepsilon}} + R^{(\tau)}_{\varepsilon}\boldsymbol{\chi}_{q^{(\tau)}_{\varepsilon}}\right)e^{-i\varepsilon t} = \sum_{\varepsilon,\tau,m}\left(A^{(\tau)}_{\varepsilon}\boldsymbol{\chi}_{p^{(\tau)}_{\varepsilon}} + B^{(\tau)}_{\varepsilon}\boldsymbol{\chi}_{q^{(\tau)}_{\varepsilon}}\right)J_m(\tfrac{V_0}{\omega})e^{-i(\varepsilon+m\omega)t} \tag{4.19}$$

Let $\varepsilon = \varepsilon_0 + s\omega$ with $s \in \mathbb{Z}$, and rearrange the summation as:

$$\begin{aligned}
&\sum_{\varepsilon_0,s,\tau}\left(c^{(I)}_{p^{(\tau)}_{\varepsilon_0+s\omega}}\boldsymbol{\chi}_{p^{(\tau)}_{\varepsilon_0+s\omega}} + R^{(\tau)}_{\varepsilon_0+s\omega}\boldsymbol{\chi}_{q^{(\tau)}_{\varepsilon_0+s\omega}}\right)e^{-i(\varepsilon_0+s\omega)t} \\
&= \sum_{\varepsilon_0,s,\tau,m}\left(A^{(\tau)}_{\varepsilon_0+s\omega}\boldsymbol{\chi}_{p^{(\tau)}_{\varepsilon_0+s\omega}} + B^{(\tau)}_{\varepsilon_0+s\omega}\boldsymbol{\chi}_{q^{(\tau)}_{\varepsilon_0+s\omega}}\right)J_m(\tfrac{V_0}{\omega})e^{-i(\varepsilon_0+s\omega+m\omega)t} \qquad (4.19)\\
&= \sum_{\varepsilon_0,s,\tau,m}\left(A^{(\tau)}_{\varepsilon_0+m\omega}\boldsymbol{\chi}_{p^{(\tau)}_{\varepsilon_0+m\omega}} + B^{(\tau)}_{\varepsilon_0+m\omega}\boldsymbol{\chi}_{q^{(\tau)}_{\varepsilon_0+m\omega}}\right)J_{s-m}(\tfrac{V_0}{\omega})e^{-i(\varepsilon_0+s\omega)t}
\end{aligned}$$

Eqn. (2.25) means the states of two energies ε_1 and ε_2 are decoupled if $(\varepsilon_1 - \varepsilon_2)/\omega \notin \mathbb{Z}$. Therefore the summation over ε_0 in Eqn. (4.19) can be omitted:

$$\sum_{s,\tau}\left(\delta_{s,0}\delta_{\tau,\tau_0}\boldsymbol{\chi}_{p^{(\tau)}_{s}} + R^{(\tau)}_{s}\boldsymbol{\chi}_{q^{(\tau)}_{s}}\right)e^{-i\varepsilon_s t} = \sum_{s,\tau,m}\left(A^{(\tau)}_{m}\boldsymbol{\chi}_{p^{(\tau)}_{m}} + B^{(\tau)}_{m}\boldsymbol{\chi}_{q^{(\tau)}_{m}}\right)J_{s-m}(\tfrac{V_0}{\omega})e^{-i\varepsilon_s t} \tag{4.20 a}$$

, with a short-hand notations that $\varepsilon_m \equiv \varepsilon_0 + m\omega$, $R_s \equiv R_{\varepsilon_0+s\omega}$, etc. Because we are interesting in the scattering between valleys, the incident wave is characterized by a single valley, τ_0 with definite energy, ε_0. Thus, the coefficients, $c^{(I)}_{p^{(\tau)}_{\varepsilon_0+s\omega}}$ is replaced by $\delta_{s,0}\delta_{\tau,\tau_0}$.

Eqn. (4.20 a) contains a set of linear equations. The other sets of equations form the rest boundary conditions are list below without derivations:

$$\sum_{s,\tau}\left(\delta_{s,0}\delta_{\tau,\tau_0}e^{-ip_s^{(\tau)}a_x}\chi_{p_s^{(\tau)}}+R_s^{(\tau)}e^{-iq_s^{(\tau)}a_x}\chi_{q_s^{(\tau)}}\right)e^{-i\varepsilon_s t}$$
$$=\sum_{s,\tau,m}\left(A_m^{(\tau)}e^{-ip_m^{(\tau)}a_x}\chi_{p_m^{(\tau)}}+B_m^{(\tau)}e^{-iq_m^{(\tau)}a_x}\chi_{q_m^{(\tau)}}\right)J_{s-m}(\tfrac{V_0}{\omega})e^{-i\varepsilon_s t} \quad (4.20\text{ b})$$

$$\sum_{s,\tau}\left(\delta_{s,0}\delta_{\tau,\tau_0}e^{ip_s^{(\tau)}La_x}\chi_{p_s^{(\tau)}}+R_s^{(\tau)}e^{iq_s^{(\tau)}La_x}\chi_{q_s^{(\tau)}}\right)e^{-i\varepsilon_s t}$$
$$=\sum_{s,\tau,m}\left(A_m^{(\tau)}e^{ip_m^{(\tau)}La_x}\chi_{p_m^{(\tau)}}+B_m^{(\tau)}e^{iq_m^{(\tau)}La_x}\chi_{q_m^{(\tau)}}\right)J_{s-m}(\tfrac{V_0}{\omega})e^{-i\varepsilon_s t} \quad (4.20\text{ c})$$

$$\sum_{s,\tau}\left(\delta_{s,0}\delta_{\tau,\tau_0}e^{ip_s^{(\tau)}(L+1)a_x}\chi_{p_s^{(\tau)}}+R_s^{(\tau)}e^{iq_s^{(\tau)}(L+1)a_x}\chi_{q_s^{(\tau)}}\right)e^{-i\varepsilon_s t}$$
$$=\sum_{s,\tau,m}\left(A_m^{(\tau)}e^{ip_m^{(\tau)}(L+1)a_x}\chi_{p_m^{(\tau)}}+B_m^{(\tau)}e^{iq_m^{(\tau)}(L+1)a_x}\chi_{q_s^{(\tau)}}\right)J_{s-m}(\tfrac{V_0}{\omega})e^{-i\varepsilon_s t} \quad (4.20\text{ d})$$

The transmission conductance and sideband structures for the time-dependent potential barrier in graphene is studied via numerically solving Eqns. (4.20) with a cut off, $|s|\le N_s$. These results are presented in **Chapter 5**.

Chapter 5
Results and discussions

In this chapter we have analyzed the conductance of a graphene with electrons normally incident to the time-dependent barrier. The results are categorized into two groups: high energy level ($E \approx t_0$) and low energy level ($|E| < 0.2t_0$).

The transmission dip structures resulting from the band top/bottom are presented in **Sec. 5-1**. We also discuss the relation between conductance and the barrier width in **Secs. 5-2** and **5-3**. In **Sec. 5-2**, an interesting phenomena we called central band refocusing (CSR) due to the interplay between Klein tunneling and linear dispersion. In **Sec. 5-3**, we demonstrate the transmission oscillating with barrier width as the incident energy lies on the dips. Such oscillation is related to Fabry-Perot resonance. However, the dips play some role and the oscillating period is double to that of ordinary Fabry-Perot experiments.

5-1 Dip structures of conductance

The transmission dips are observed as one of the sidebands lies close to band top/bottom. The physics origin of the dips is the diverse of density of state at band top/bottom. Besides, the current of these states are close to zero. Therefore, if one of the sidebands near band top/bottom, the transmission to this sideband is enhanced and the electrons are trapped within this sideband.

For gapped graphene, the band top/bottom naturally exist in low energy regime. **Figs. 5.1** and **5.3** show there are two dips which relate to conductance band bottom ($E = \Delta$) and valance band top ($E = -\Delta$) respectively. Figs. 5.2 and 5.3 also reveal the difference between $\hbar\omega = 2\Delta$ (**Fig. 5.1**) and $\hbar\omega \geq 2\Delta$ (**Fig. 5.3**). For gapless graphene, the band top/bottom are at energy t_0 ($-t_0$) and **Fig. 5.5** shows the transmission dips relating to band top ($E = t_0$). **Fig. 5.7** shows the number of sideband we take into consideration would affect the accuracy of results.

In case of the wrong data we may get, we introduce a way to calculate the accuracy by testing the current conservation. Where N is the amount of data, i label the region of current, see Fig 4.1. For instance, $N = 100$ means we have 100 data and $i = 2$ means the II region of current is considered.

$$\sigma_J = \sqrt{\frac{1}{3N}\sum_{j}^{N}\sum_{i}^{3}\left(J_{ij} - \bar{J}_j\right)^2}$$

Effective density of state fixing ky can be written as

$$D(\varepsilon)=\frac{dN}{d\varepsilon}=\left(\frac{L}{2\pi}\right)^2\frac{\sqrt{\Delta^2+4\cos(k_xa_x)+4\cos^2(k_xa_x)}}{-4a\left[\sin(k_xa_x)-2\cos(k_xa_x)\sin(k_xa_x)\right]}$$

Effective density of state will go to infinity when k_x is at Dirac cone.

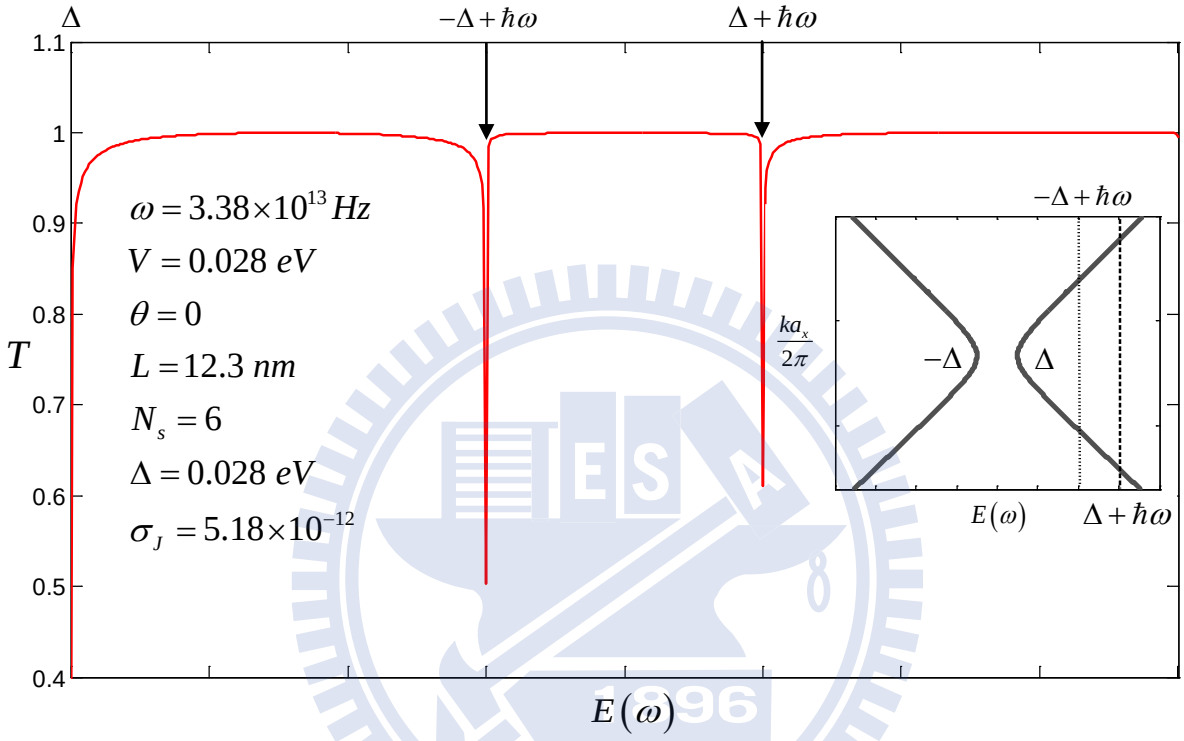

Fig. 5.1. The transmission dips appear when the incident Energy is $1\hbar\omega$ away from the band edges Δ and $-\Delta$ which have large effective density of state by fixing ky. L refers to the width of barrier. σ_J indicates the degree of accuracy. The arrows show that incident energies $-\Delta+\hbar\omega$ and $\Delta+\hbar\omega$ emit a photon with $\hbar\omega$ and be trapped at valence/conduction band edge.

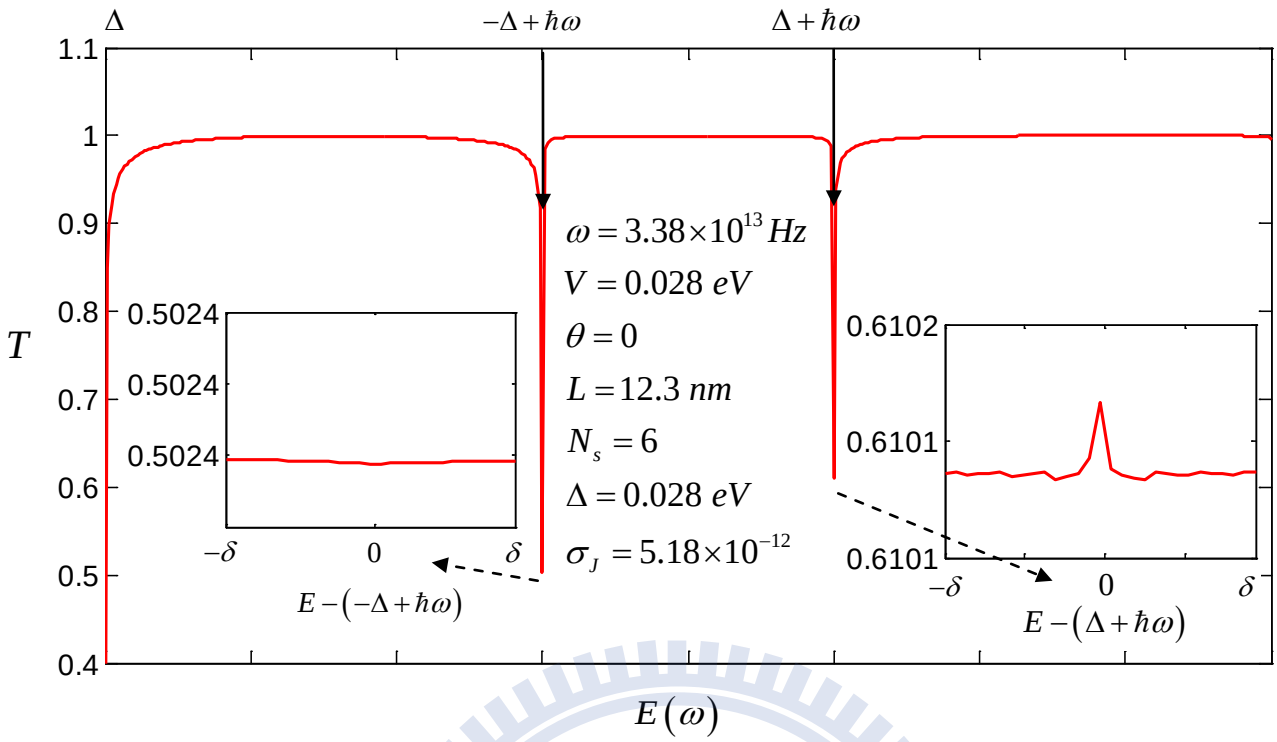

Fig. 5.2. Shown in the two inserts are blow-ups of the *T*-*E* curves near the vicinity of the two dip structures in Fig. 5.1. Here $\delta = 10^{-15}\ \hbar\omega$. Whereas the figures show that *T* do not drop to zero at the two dip structures, they confirm that we have found the two minimum *T* values.

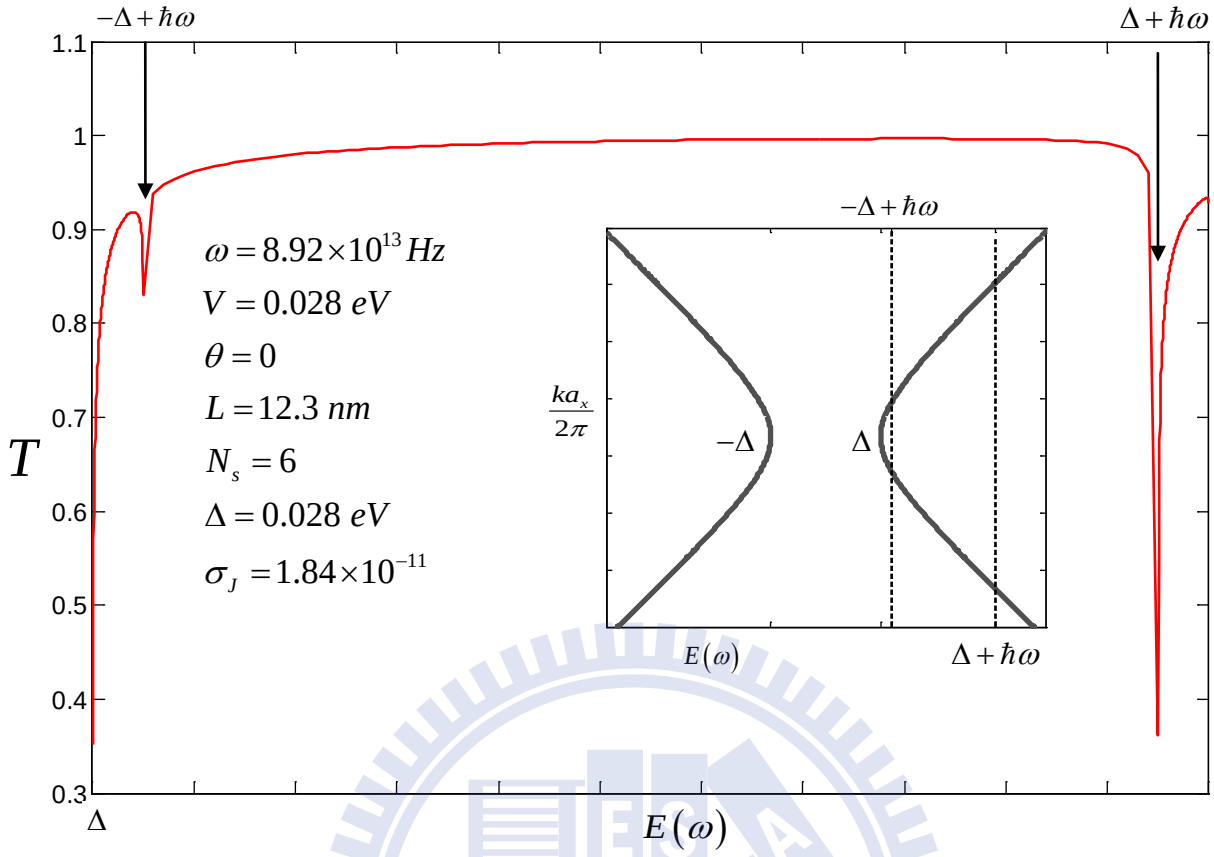

Fig. 5.3. The transmission dips appear when the incident Energy is $1\,\hbar\omega$ away from the band edges Δ and $-\Delta$ which have large effective density of state by fixing ky. L refers to the width of barrier. σ_J indicates the degree of accuracy.

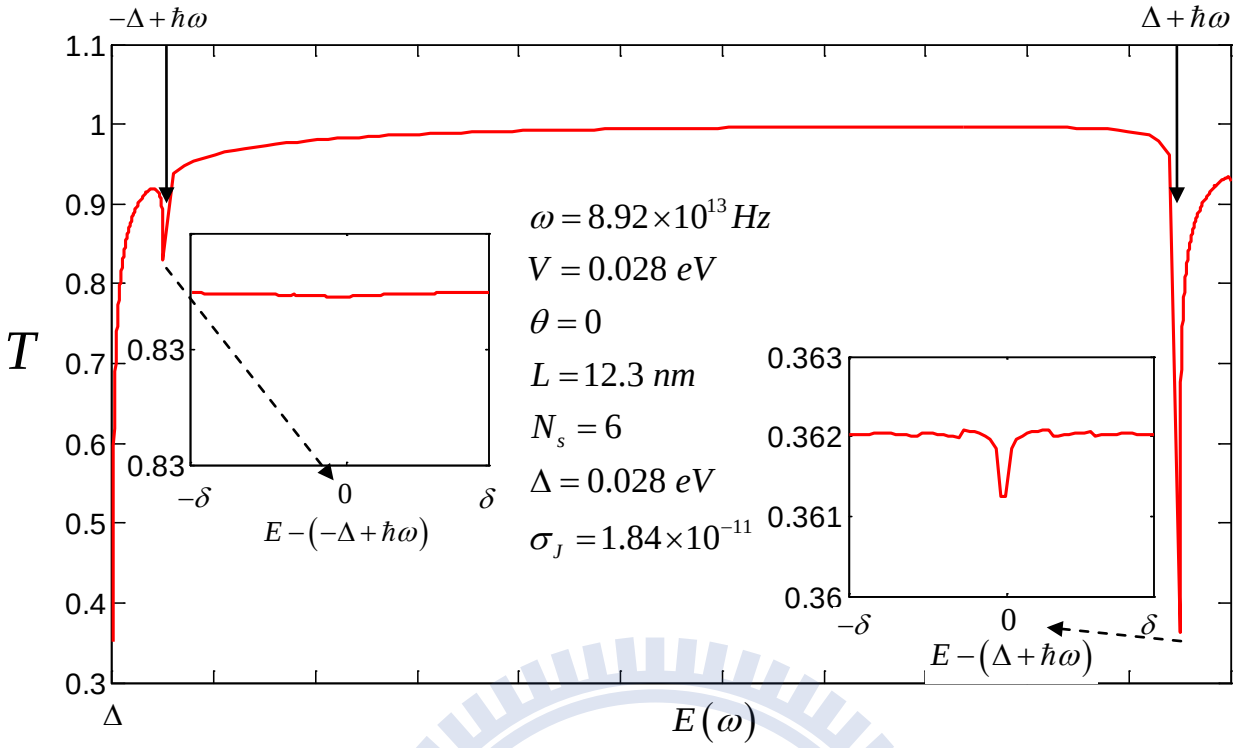

Fig. 5.4. Shown in the two inserts are blow-ups of the *T*-*E* curves near the vicinity of the two dip structures in Fig. 5.3. Here $\delta = 10^{-15}\ \hbar\omega$.

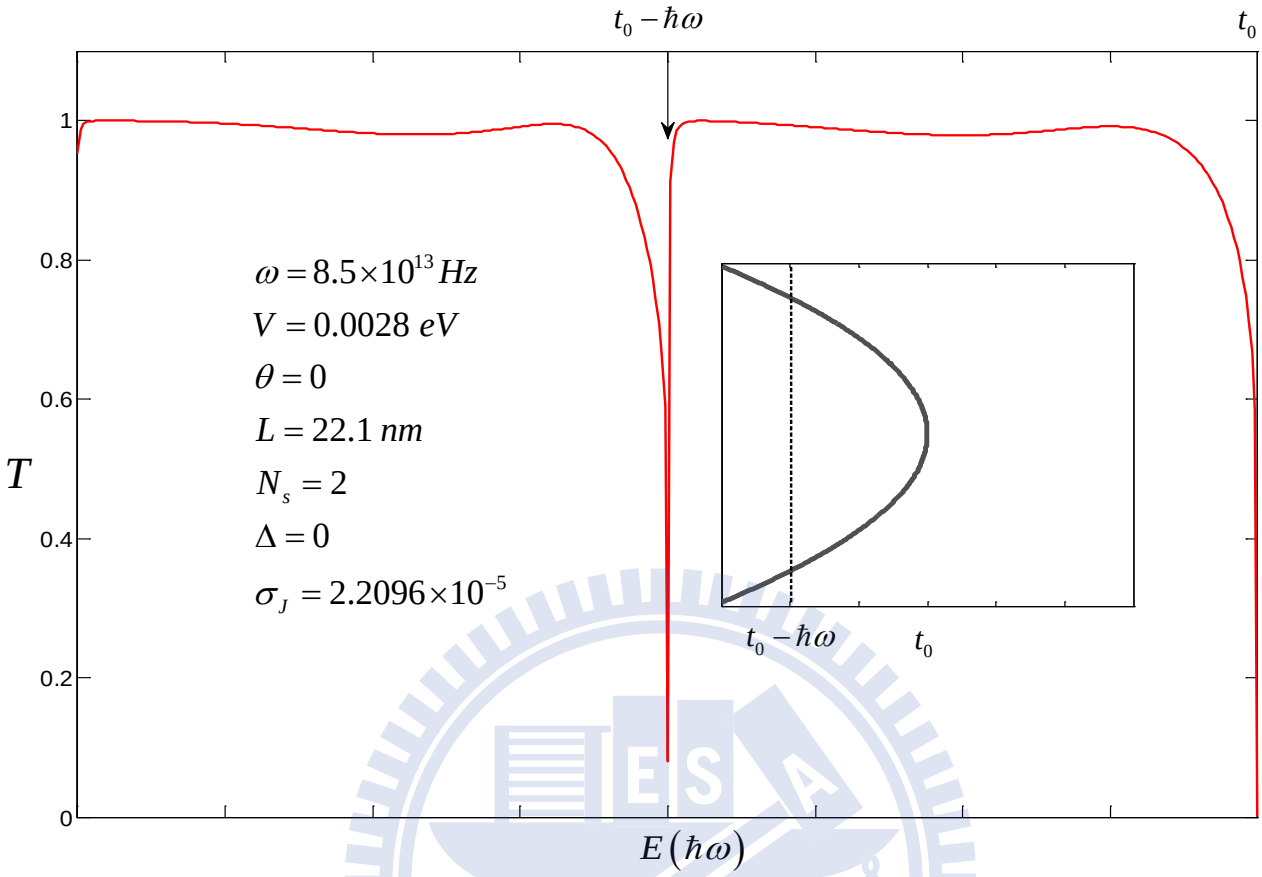

Fig. 5.5. The transmission dips appear when the incident Energy is $1\hbar\omega$ away from the band edges E_2 which have large effective density of state by fixing ky. L refers to the width of barrier. σ_J indicates the degree of accuracy.

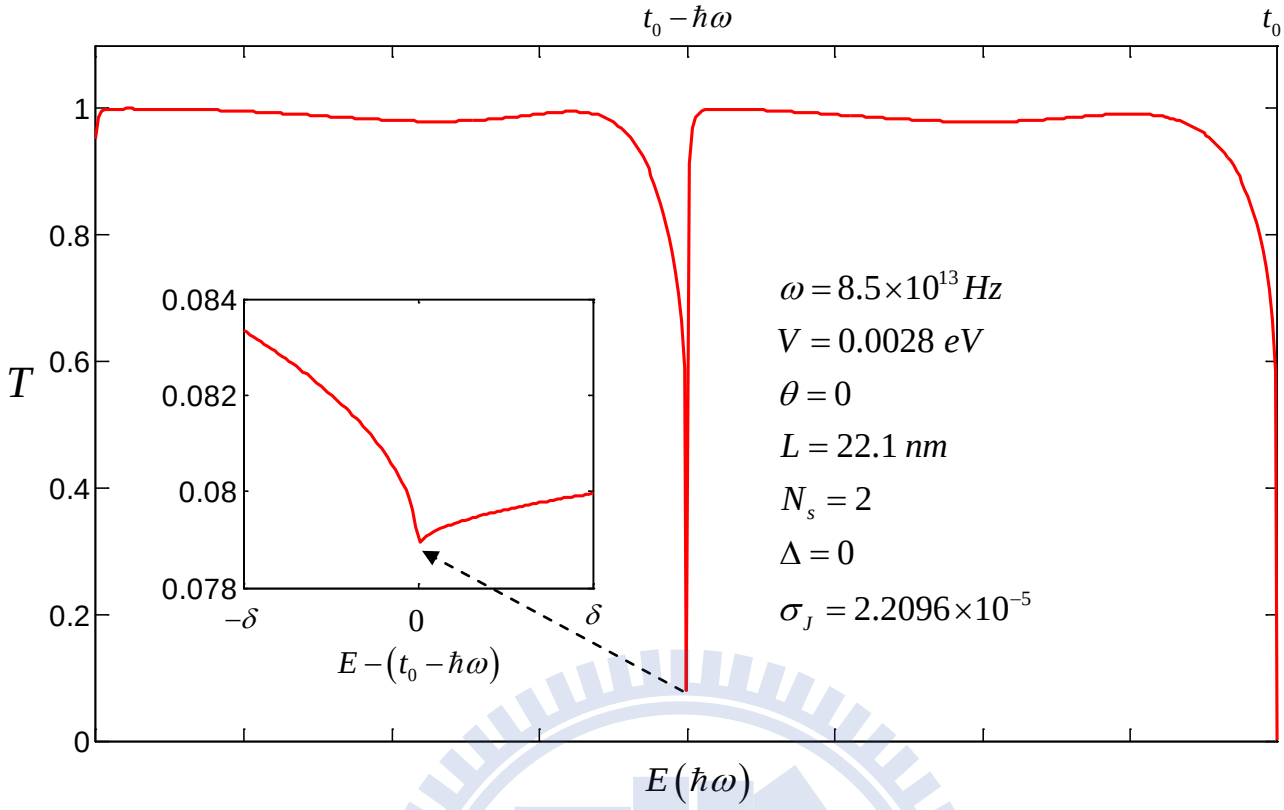

Fig. 5.6. Shown in the insert is a blow-up of the *T-E* curve near the vicinity of the dip structure in Fig. 5.5. Here $\delta=10^{-15}\ \hbar\omega$.

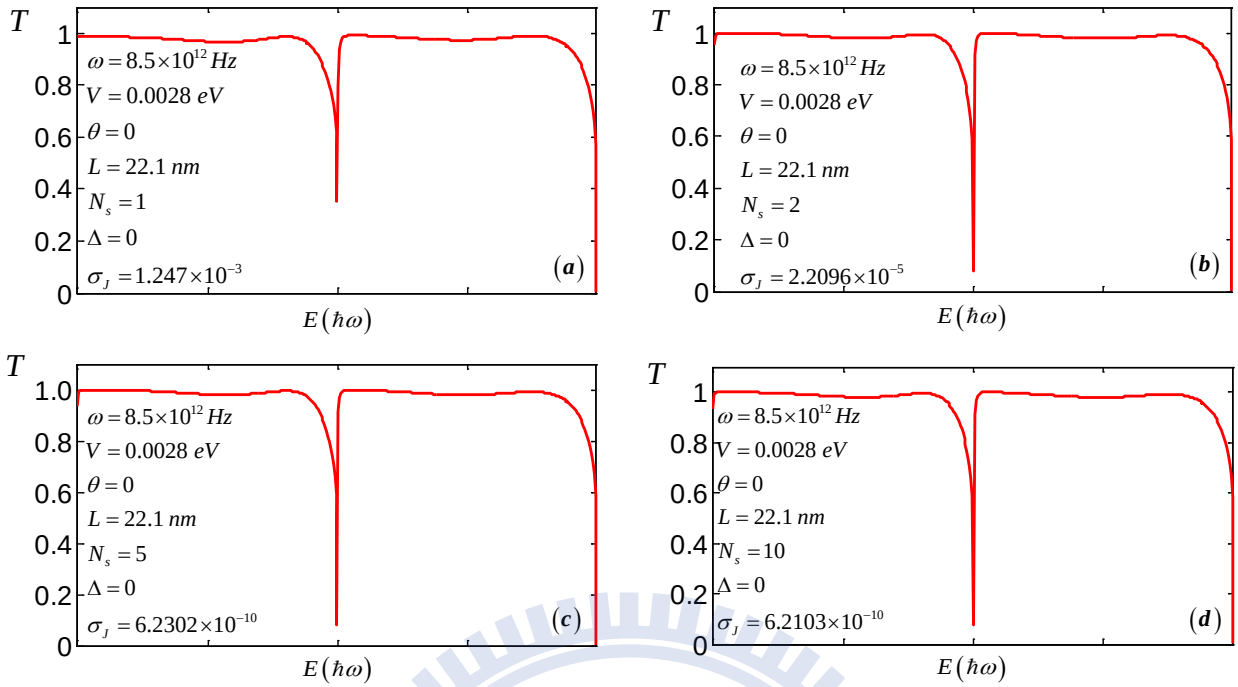

Fig. 5.7. Numerical convergence of our calculation is shown when the number of sidebands N_s included in our calculation is increased systematically, with $N_s = 1,\ 2,\ 5,\ 10$, respectively, in Figs. 5.7(a)-(d). Correspondingly, both the accuracies σ_J and the *T-E* curves improve rapidly and converge nicely in Fig. 5.7 (d).

5-2 Central band refocusing (CSR)

In this section, the relation between transmission and barrier width is investigated in the low energy regime. An exotic phenomenon, the central band refocusing (CSR), is observed that the transmission can be periodical dominated by the central band as the barrier width increasing. **Fig. 5.5** shows the CSR profile, the total transmission is fixed at one due to the Klein tunneling. However, the transmission via other sidebands oscillate with the barrier width. The phenomena of CSR is established by three elements: (1) the Klein tunneling, (2) nearly null inter-valley scattering, and (3) linear dispersion. The first two factors forbid any reflection waves that only the central band exists in Region *I*. The other sidebands are allowed in Region *II* with only forward wave vectors (null inter-valley transition and Klein tunneling). More specifically, Eqns. (5.1) and (5.2) are the wave functions for Region *I* and Region *II* with the incident wave at K_1 valley and energy E_0:

$$\boldsymbol{F}_M^{(I)}(t)=\tfrac{1}{\sqrt{N}}\sum_{m,\tau}\left(e^{ip_m^{(1)}Ma_x}\chi_{p_m^{(1)}}\delta_{m,0}+R_m^{(\tau)}e^{iq_m^{(\tau)}Ma_x}\chi_{q_m^{(\tau)}}\right)e^{-iE_mt}=\tfrac{1}{\sqrt{N}}e^{ip_0^{(1)}Ma_x}\chi_{p_0^{(1)}}e^{-iE_0t} \tag{5.1}$$

$$\begin{aligned}\boldsymbol{F}_M^{(II)}(t)&=\tfrac{1}{\sqrt{N}}\sum_{\tau,m,s}\left(A_s^{(\tau)}e^{ip_s^{(\tau)}Ma_x}\chi_{p_s^{(\tau)}}+B_s^{(\tau)}e^{iq_s^{(\tau)}Ma_x}\chi_{q_s^{(\tau)}}\right)J_{m-s}(\tfrac{V_0}{\omega})e^{-iE_mt}\\&=\tfrac{1}{\sqrt{N}}\sum_{m,s}\left(A_s^{(1)}e^{ip_s^{(1)}Ma_x}\chi_{p_s^{(1)}}+A_s^{(2)}e^{ip_s^{(2)}Ma_x}\chi_{p_s^{(2)}}\right)J_{m-s}(\tfrac{V_0}{\omega})e^{-iE_mt}\\&=\tfrac{1}{\sqrt{N}}\sum_{m,s}A_s^{(1)}e^{ip_s^{(1)}Ma_x}\chi_{p_s^{(1)}}J_{m-s}(\tfrac{V_0}{\omega})e^{-iE_mt}\end{aligned} \tag{5.2}$$

The coefficients, $A_s^{(1)}$, are determined via Eqn. (4.17 a), only (the difference between Eqns (4.17 a) and (4.17 b) is the same order with that of the inter-valley scattering. That is they are identical in the sense of absence of inter-valley scattering.). Therefore these $A_s^{(1)}$-coefficients are irrelevant to the boundaries at $M=L$ and $L+1$. Furthermore, Eqn. (4.17 a) forces the wave function of the sideband components other than central band are zero at $M=0$.

The above discussions only complete the half of the story. The other half is from the linear dispersion that the wave vectors for different sidebands are characterized by:

$$p_m^{(1)}=p_0^{(1)}+m\Delta p$$

, where $p_0^{(1)}$ is the wave vector of the central band and $p_m^{(1)}$ that of the m-th sideband with energy $E_m=E_0+m\hbar\omega$. Hence, the wave function in Region *II* is periodic with the period determined by $2\pi/\Delta p=2\pi\hbar\omega/v_F$.

Fig. 5.9 shows the absolute wave function components for individual sidebands for the cases of

two different width of potential, L=250 and L=500. It demonstrates that the coefficients of $A_s^{(1)}$ are determined, only, by left boundary of the barrier.

Fig. 5.10 shows how different V affect CSR. Compare to **Fig. 5.8**, we double the amplitude of barrier, we find that the contribution to conductance is separated by more sidebands and the period does not change.

Fig. 5.11 shows how different ω affect CSR. Compare to **Fig. 5.8**, we have one-half frequency; we find that not only the contribution to conductance which is separated by more sidebands, the period is also double.

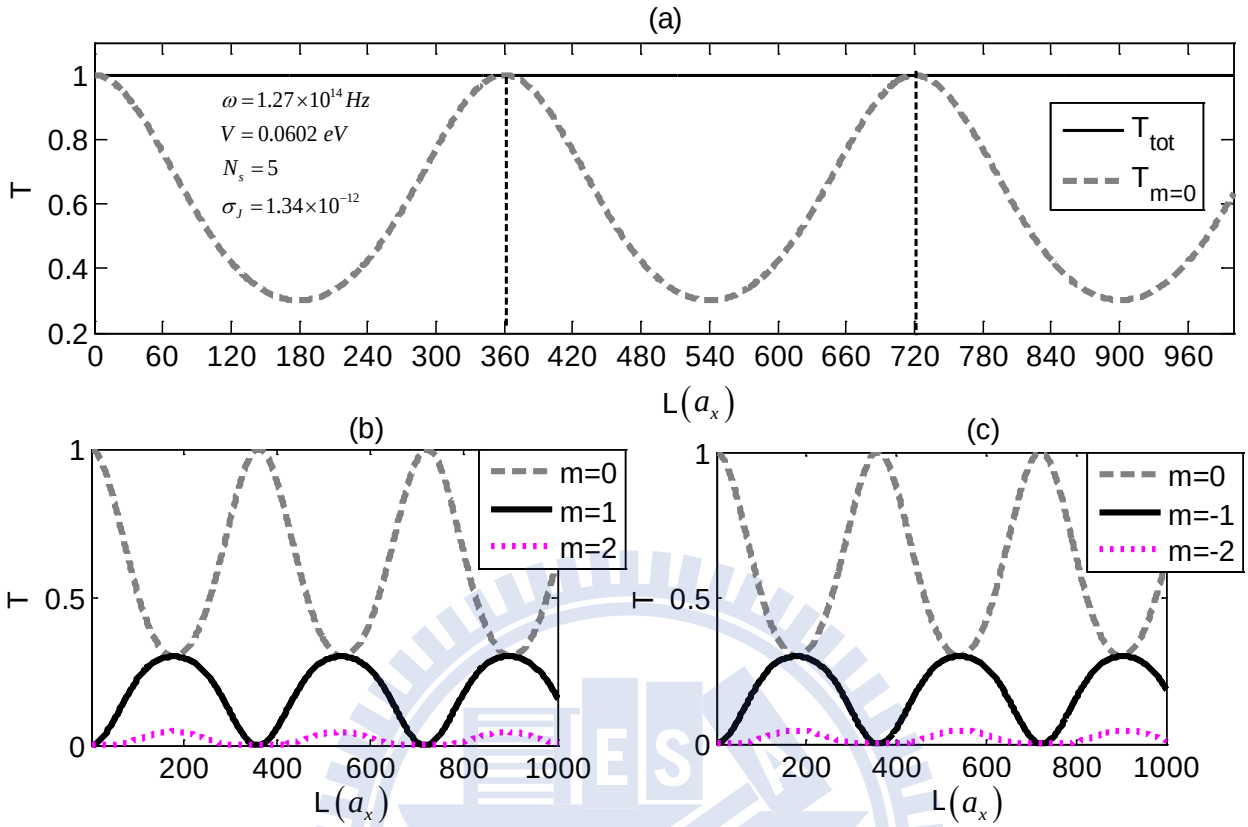

Fig. 5.8 (a) Central band refocusing (CSR) profile. The period of oscillated sideband conductance can only determined by the difference between forward wave vectors which are $k_m - k_0$ $(m = \pm 1)$. **(b)** Compare central band with sidebands which absorb photons. **(c)** Compare central band with sidebands which emit photons. The Δ=0 means this system is a gapless graphene. L refers to the width of barrier in unit of a_x. σ_J indicate the degree of accuracy.

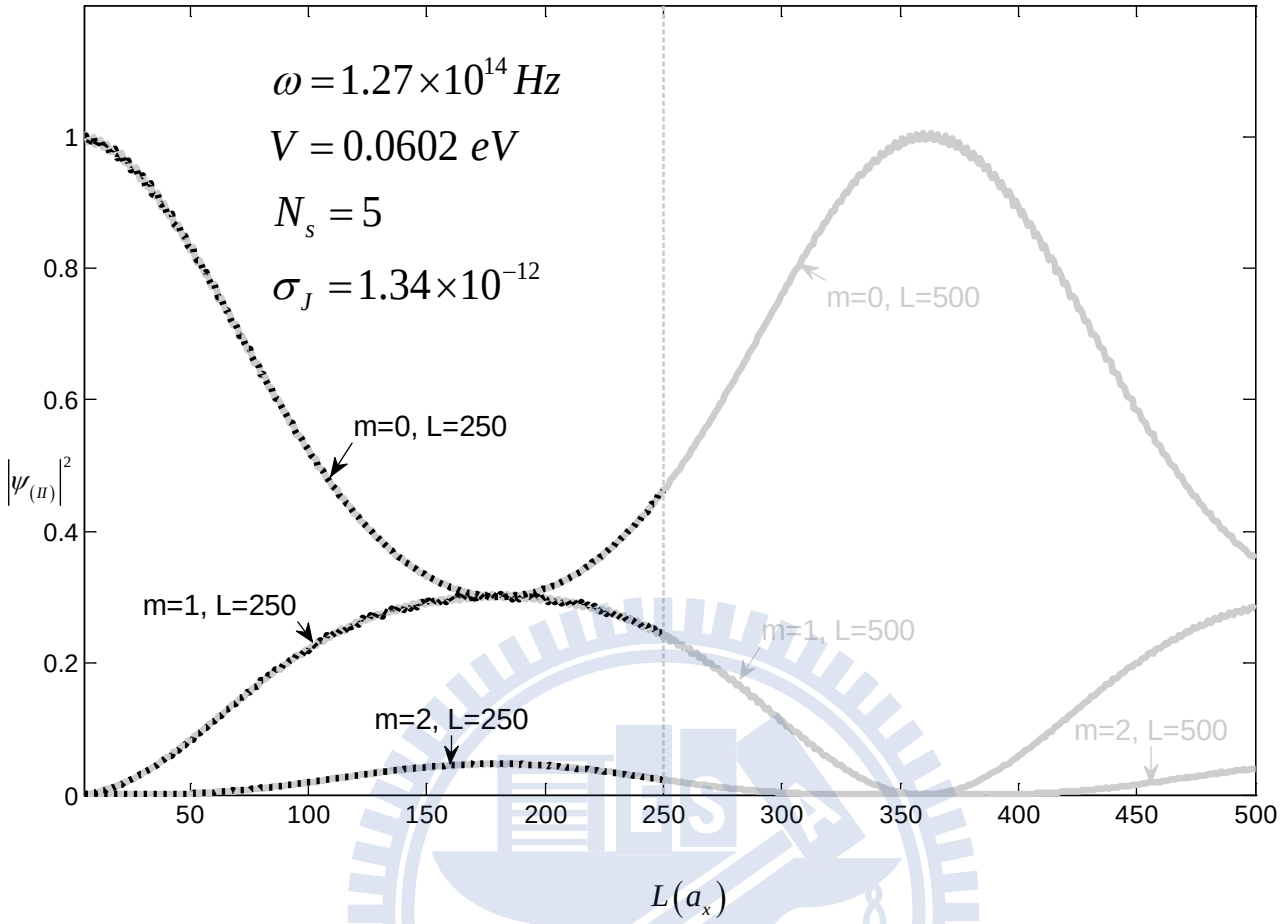

Fig. 5.9 the densities of individual sidebands in Region *II* with two barrier widths, *L*=240 and *L*=500.

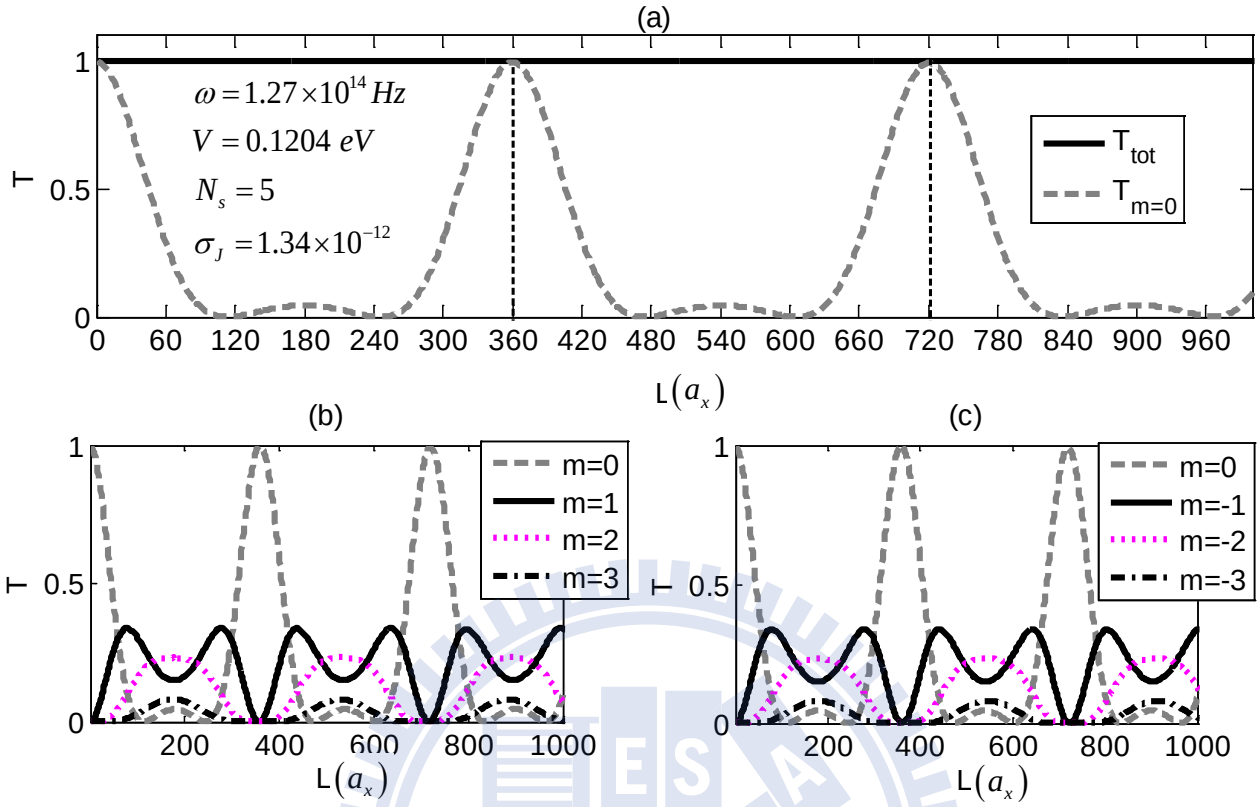

Fig. 5.10 (a) Central band refocusing (CSR) profile applying with double amplitude of time-dependent potential. The period of oscillated sideband conductance can only determined by the difference between forward wave vectors which are $k_m - k_0 \ \ (m = \pm 1)$.**(b)** Compare central band with sidebands which absorb photons. **(c)** Compare central band with sidebands which emit photons. The Δ=0 means this system is a gapless graphene. L refers to the width of barrier in unit of a_x. σ_J indicate the degree of accuracy.

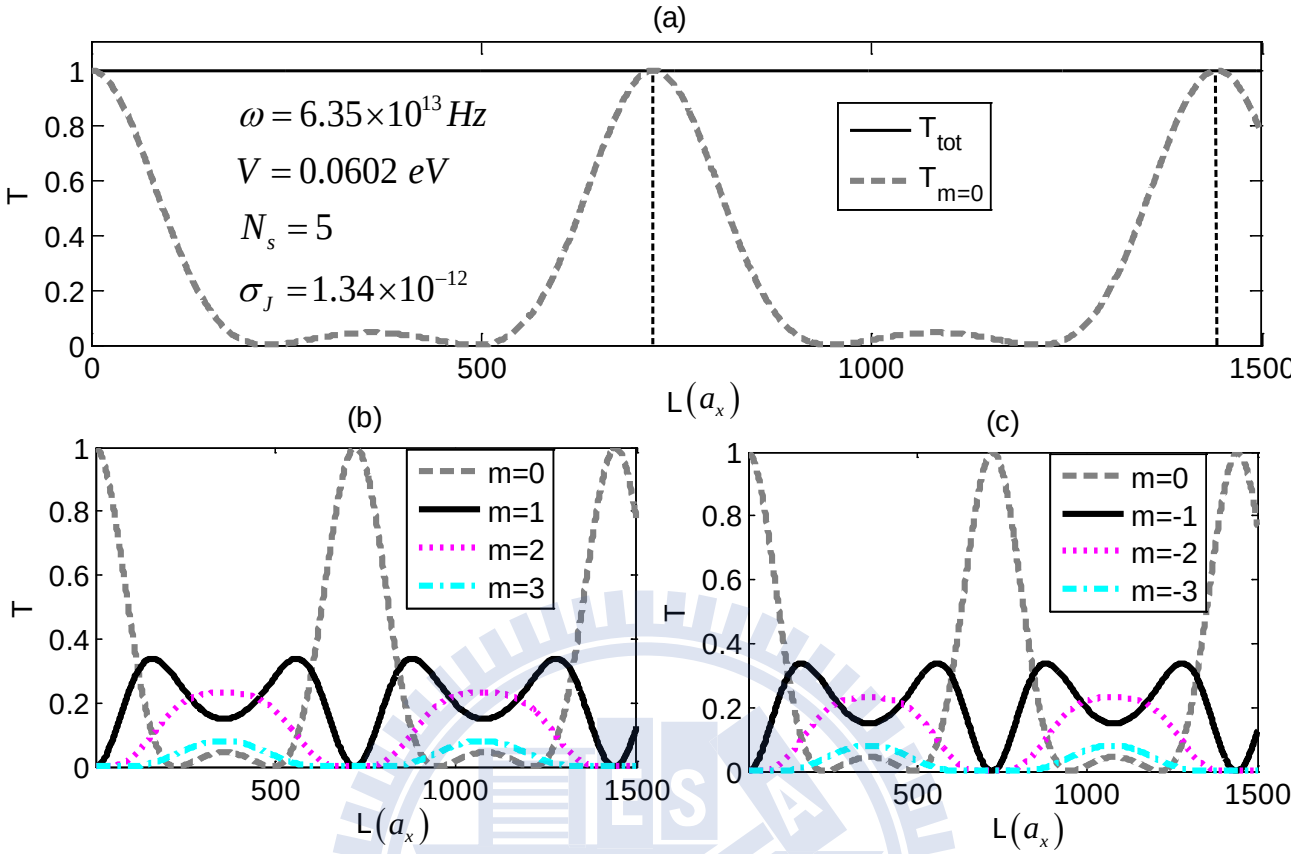

Fig. 5.11 (a) Central band refocusing (CSR) profile applying with frequency is one-half of that in **Fig. 5.6**. The period of oscillated sideband conductance can only determined by the difference between forward wave vectors which are $k_m - k_0$ $(m = \pm 1)$.**(b)** Compare central band with sidebands which absorb photons. **(c)** Compare central band with sidebands which emit photons. The Δ=0 means this system is a gapless graphene. L refers to the width of barrier in unit of a_x. σ_J indicate the degree of accuracy.

5-3 Non-typical Fabry-Perot resonance

In this section, we present the Fabry-Perot resonance as the incidence energy lies on dips. For the dips enhance reflection, the interference between forward and backward waves takes place inside the region of potential barrier. To simplify the analysis, the parameters are specified such that transmissions and reflections are dominated by two sidebands.

Fig. 5.12 displays the Fabry-Perot resonance with *K*-valley incident and the 1st sideband energy, $E_1 = E_0 + \hbar\omega = t_0$. The transmission is dominated by central band and the oscillating period is determined from the difference between wave vectors in the central band, $2\pi / (q_0^{(2)} - p_0^{(1)}) = 26.5a_x$. However, the period is $53a_x$, double to that of estimated.

Also we can observe the dip structure by selecting certain barrier width in Fig. 5.8. In **Fig. 5.13** we give a series of dip structure by varying with barrier width. It is interesting that we can control the dip structure to be survived or not. We can reopen the Klein-tunneling; we can make zero transmission as well by choosing certain barrier width.

Fig. 5.14 demonstrates the Febry-Perot resonance for gapped graphene at low energy region with size of gap = 2Δ. The incident wave is at *K*-valley and the next sideband energy lies on the conduction band edge ($E_{-1} = E_0 - \hbar\omega = \Delta$).

$$\omega = 5.95\times10^{13}\ Hz,\quad V = 0.0084\ eV$$
$$\theta = 0,\ \Delta = 0,\ N_s = 2,\ \sigma = 5.64\times10^{-5}$$

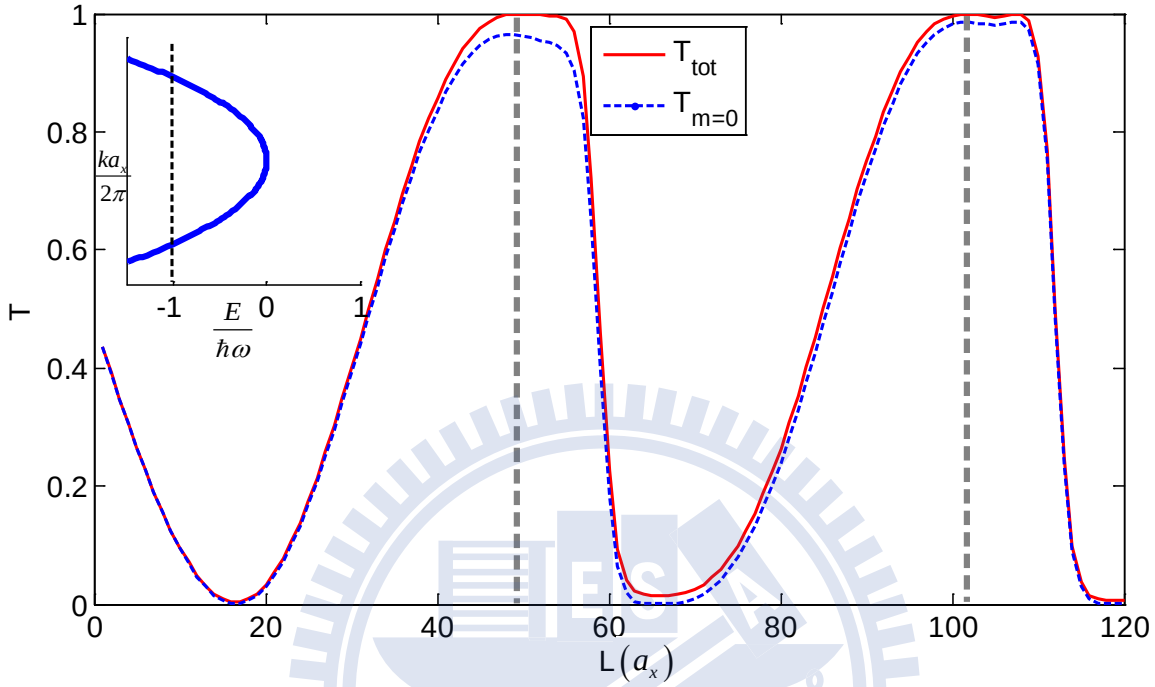

Fig. 5.12 Non-typical Fabry-Perot resonance for the case when the incident energy stays at the dip structure. The incidence energy $E_0 = t_0 - \hbar\omega$ is at an $\hbar\omega$ below the band top t_0. The choice of the time-modulated potential parameters are such that only up to first-sideband processes are important. The curve shows the dominance of the central band in the transmission. The L-period cannot be explained by the usual Fabry-Perot resonance condition: $2\pi / (q_0^{(2)} - p_0^{(1)}) = 26.5a_x$, where $q_0^{(2)}$, $p_0^{(1)}$ are wavevector-pairs for the elastic channel. It is explained by a non-typical Fabry-Perot resonance that connects wavevector-pairs between the central and the first-sideband channels.

$$\omega = 5.95\times10^{13}\ Hz,\ V = 0.0084\ eV$$
$$\theta = 0,\ \Delta = 0,\ N_s = 2,\ \sigma = 5.64\times10^{-5}$$

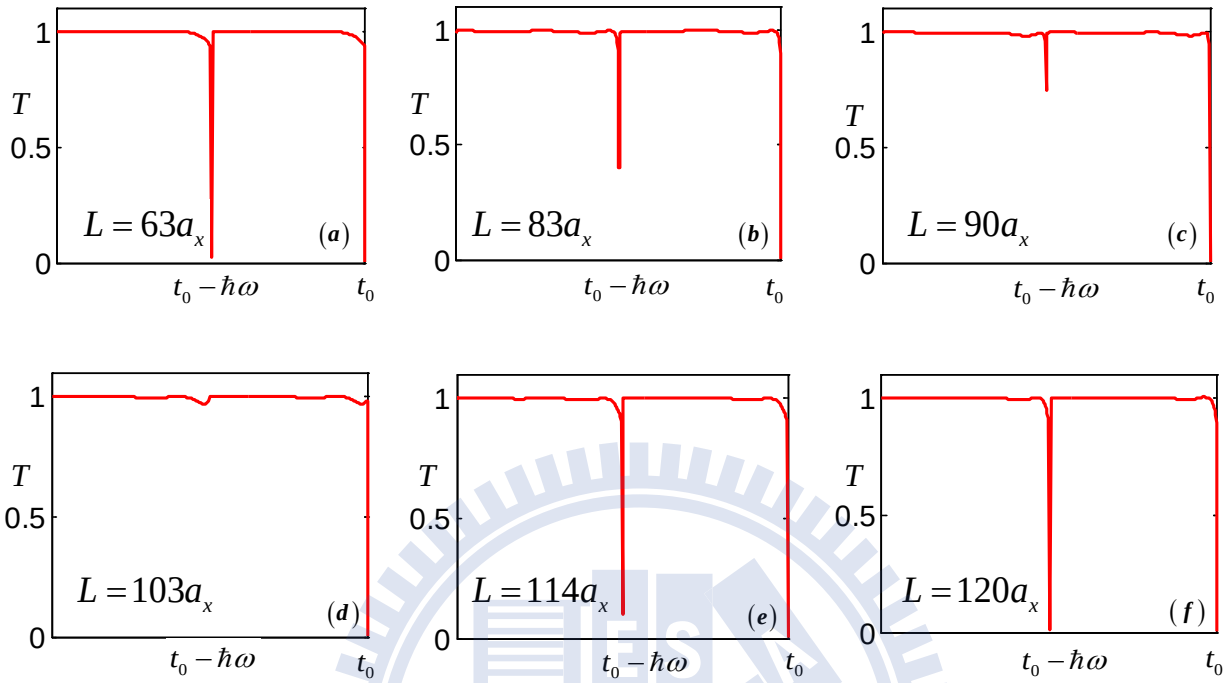

Fig. 5.13 *T-E* curves for selected *L* values in Fig. 5.12, which show that the dip structures can be fine-tuned by *L*.

$\omega = 5.95\times10^{13}\ Hz,\ V = 0.0028\ eV$

$\theta = 0,\ \Delta = 0.028\ eV,\ N_s = 5,\ \sigma = 1.34\times10^{-12}$

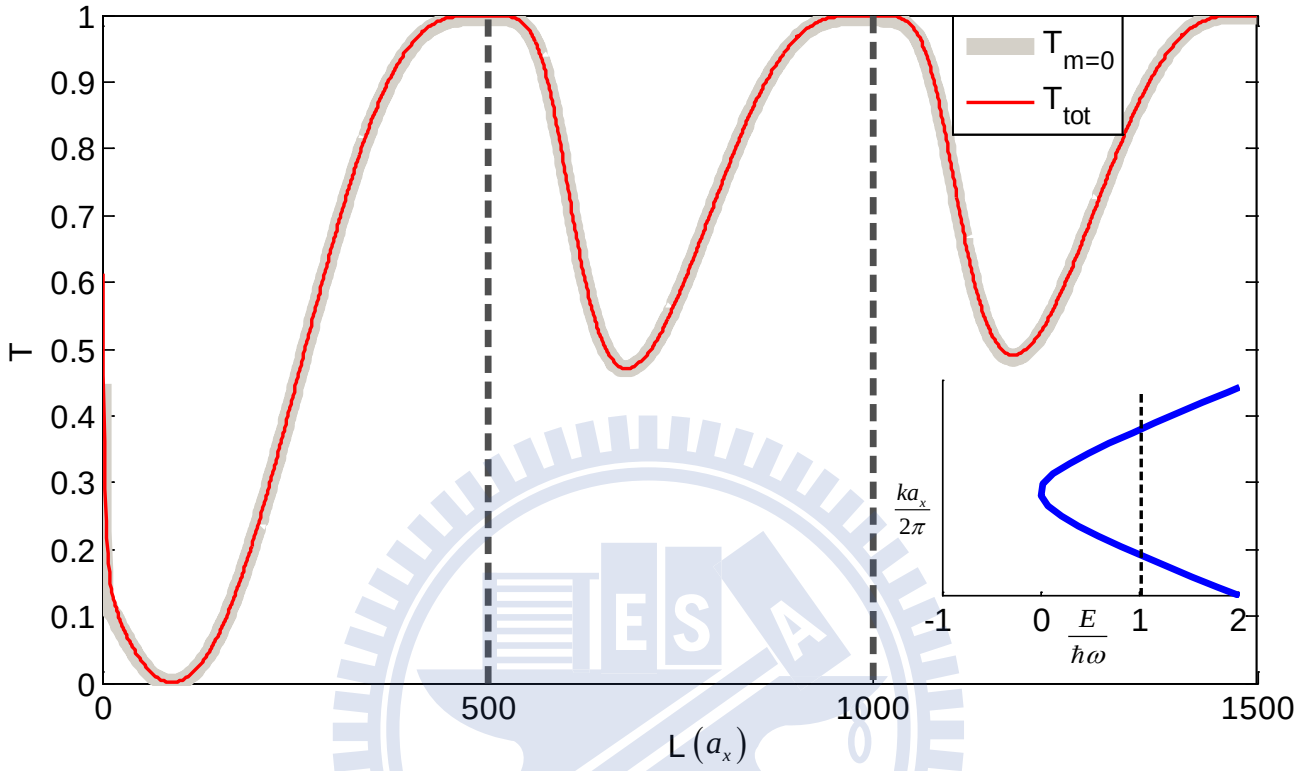

Fig. 5.14 Non-typical Fabry-Perot resonance for the case when the system stays at the dip structure, with low incident energy, and the graphene is gapped . The incident energy $E_0 = \Delta + \hbar\omega$ is at an $\hbar\omega$ above the band bottom Δ. The observed physics in Fig. 5.12 remain valid here. The *L*-period is the result of a non-typical Fabry-Perot resonance condition.

Appendix A

The x component of momentum we choice in calculation is quite important. By Eqn.(A1) we can get four momentum by given energy and k_y. Two is for forward propagating mode, the other two is for backward propagating mode.

$$k_x = \frac{1}{a_x}\cos^{-1}\left(\frac{-\cos k_y a_{2y} \pm \sqrt{E^2 - \sin^2\left(k_y a_{2y}\right)}}{2}\right)$$

In the following discussion we replace k_x with p and q to present the forward and backward propagating momentum, respectively.

Momentums can be divided into two parts. One is real part and the other one is imaginary part. The sign of real part decide which valley the momentum belongs to. We set up τ as valley index. Here the valley index was accompany with momentum $p^{(\tau)}$, we define $p^{(1)}$, $q^{(1)}$ ($p^{(2)}$, $q^{(2)}$) as $K\left(K'\right)$ valley.

The sign of imaginary part should be treated very carefully to prevent explosion from wave function. It should be positive when the real part of momentum is positive and be negative when the real part of momentum is negative. For example, in Eqn.(A2) if the imaginary part of p is negative, then $e^{ip^{\eta}{}_{m}Ma_x}$ will come to be infinity while M is increasing. However, it is wrong because when the wave is propagating within potential area, it should be decay while the propagating distance is increasing.

$$\psi^{(II)}(M;t) = \sum_{m,l,\tau}\left[a_l^{\tau} J_{m-l}(z) e^{iMp^{(\tau)}a_x}\begin{pmatrix} c_A(p_l^{(\tau)}) \\ c_B(p_l^{(\tau)}) \end{pmatrix} + b_l^{\tau} J_{m-l}(z) e^{iMq^{(\tau)}a_x}\begin{pmatrix} c_A(q_l^{(\tau)}) \\ c_B(q_l^{(\tau)}) \end{pmatrix}\right] e^{-iE_m t} \qquad \text{(A2)}$$

There are two cases, which have different dispersion energy profile owing to $k_y a_y > \frac{\pi}{2}$ and $k_y a_y < \frac{\pi}{2}$ according to Eqn.(A.1). Hence, the dispersion confined in Brillouin zone will be discussed separately. The different energy levels also lead to different scenario, which need to be discussed individually.

Case(a): $k_y a_y < \frac{\pi}{2}$

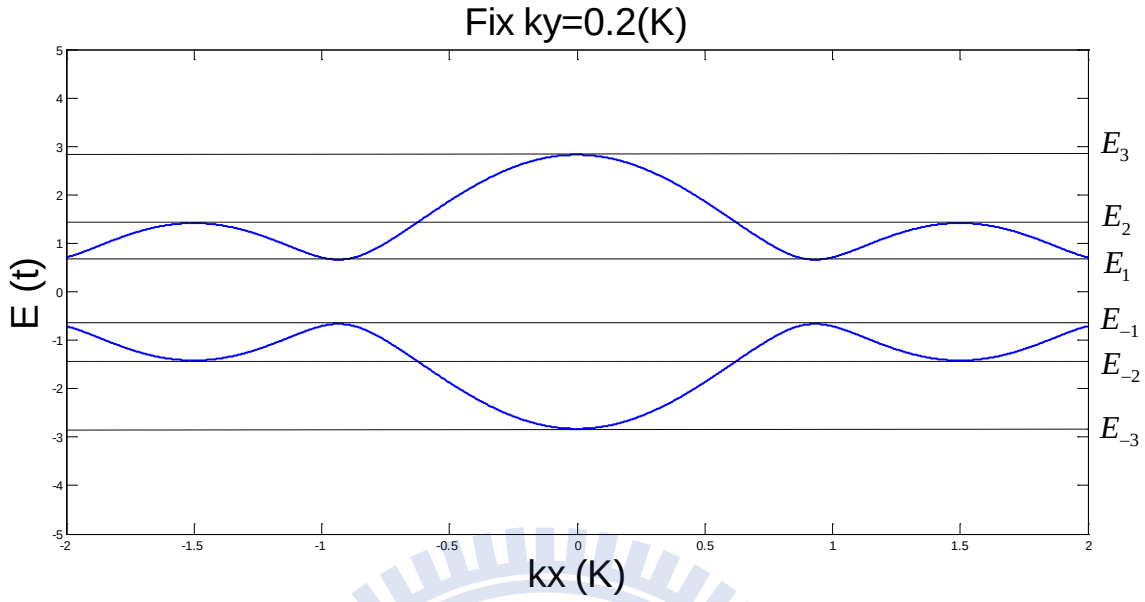

Fig.A.1: Case(a) Energy dispersion fixing $k_y = 0.2(K)$ which means $k_y a_y < \frac{\pi}{2}$. The band bottom is flat. The dashed lines divide energy levels into different scenario, which need to be discussed individually. We will get 4 momentum from Eqn(A.1). In regions $E_{-1} < E < E_1$, $E > E_3$, $E < E_{-3}$ we get 4 complex wave vectors. In regions $E_2 < E < E_3$, $E_{-3} < E < E_{-2}$ we get 2 complex 2 real wave vectors. In regions $E_1 < E < E_2$, $E_{-2} < E < E_{-1}$ we get 4 real wave vectors. We define that if k_x is positive corresponding to the energy region we focus on then we name it K-related wave vector, contrary to K related wave vector if k_x is negative then we name it K'-related wave vector. And we define right-going wave vector as p left-going wave vector as q. Here the valley index was accompany with momentum $p^{(\tau)}$, we define $p^{(1)}, q^{(1)}$ ($p^{(2)}, q^{(2)}$) as $K\,(K')$ valley. X-axis is momentum k_x in unit of $K = \frac{4\pi}{3\sqrt{3}a_0}$;Y-axis is energy in unit of $t_0 = 2.8ev$.

$E_1 = \sin(k_y a_y), E_2 = \sqrt{5 - 4\cos(k_y a_y)}, E_3 = \sqrt{5 + 4\cos(k_y a_y)}, E_{-1} = -E_1$, $E_{-2} = -E_2$, $E_{-3} = -E_3$

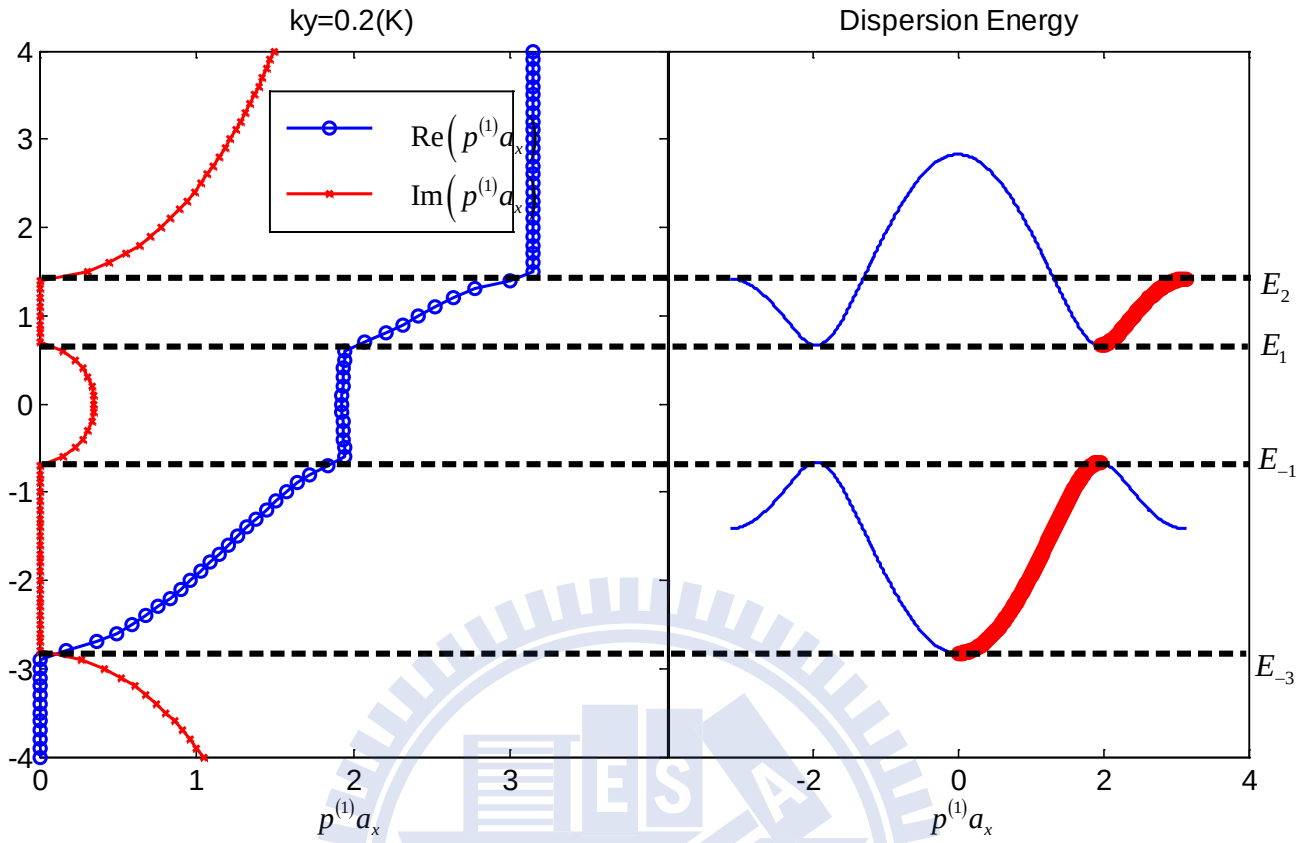

FigA.2.Left: Plot momentum $p^{(1)}$ in real(Blue circle) and imaginary(Red cross) part. Fix k_y at 0.2K. Right: Energy dispersion, which used to compare with the left figure. The red line label the momentum we are discussing. According to energy dispersion plot with red line, the group velocity is always positive. In regions $E > E_2$, $E < E_{-3}, E_{-1} < E < E_1$ $p^{(1)}$ is given by evanescent mode.

In regions of $E_1 \le E \le E_2, E_{-3} < E < E_{-1}$, $p^{(1)}$ is given by propagating mode. The imaginary part of $p^{(1)}$ become larger as the energy is further away from the band bottom, and become smaller as the energy is closer toward to the band bottom.

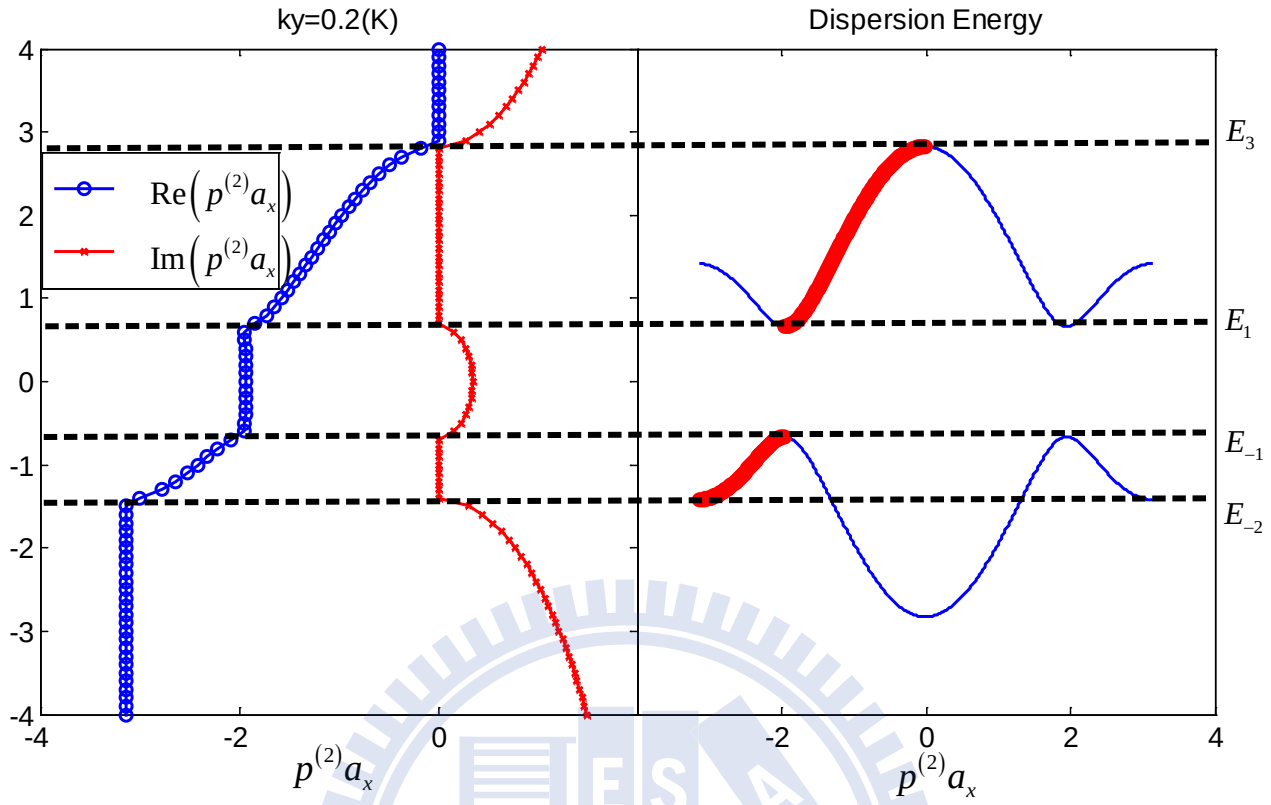

Fig. A.3.Left: Plot momentum $p^{(2)}$ in real(Blue circle) and imaginary(Red cross) part. Fix k_y at 0.2K.

Right: Energy dispersion, which used to compare with the left figure. The red line label the momentum we are discussing. According to energy dispersion plot with red line, the group velocity is always positive. In regions $E < E_{-2}$, $E > E_3$, $E_{-1} < E < E_1$ $p^{(2)}$ is given by evanescent mode. In regions $E_1 \le E \le E_3$, $E_{-2} < E < E_{-1}$, $p^{(2)}$ is given by propagating mode. The imaginary part of $p^{(2)}$ become larger as the energy is further away from the band bottom, and become smaller as the energy is closer toward to the band bottom.

Case(b): $k_y a_y > \frac{\pi}{2}$

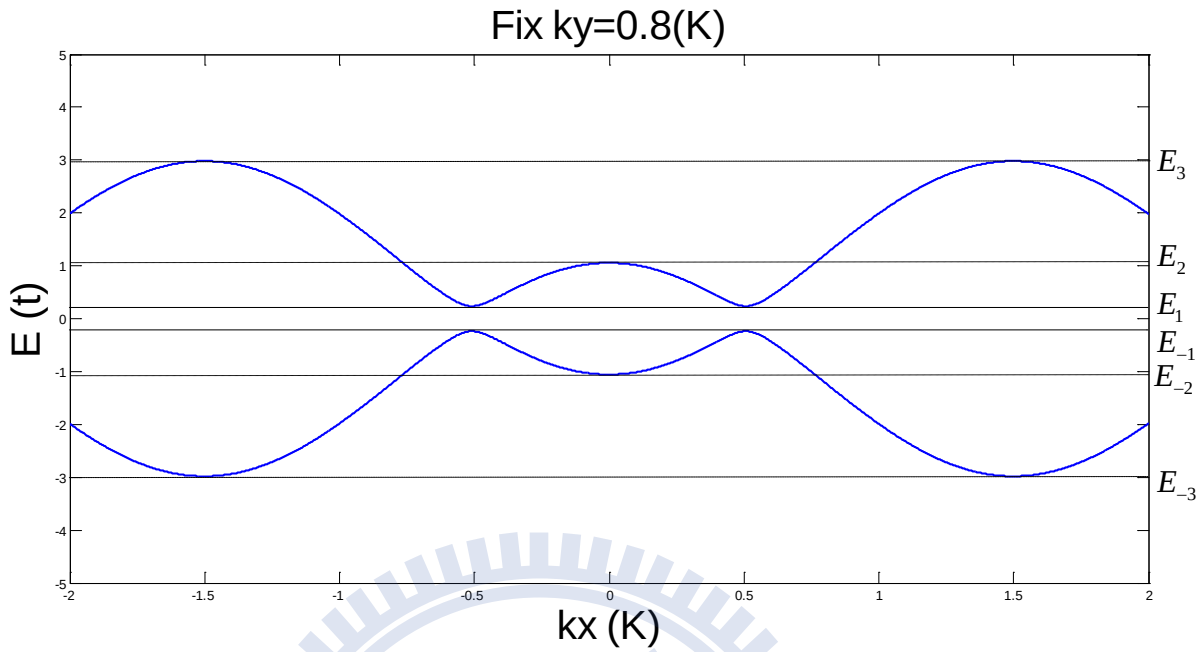

Fig.A.4 Energy dispersion fixing $k_y = 0.8(K)$ which means $k_y a_y > \frac{\pi}{2}$. The band bottom is flat.

The dashed lines divide energy levels into different scenario, which need to be discussed individually. We will get 4 wave vector from Eqn.(A.1). In regions $E_{-1} < E < E_1$, $E > E_3$, $E < E_{-3}$ we get 4 complex wave vectors. In regions $E_2 < E < E_3$, $E_{-3} < E < E_{-2}$ we get 2 complex 2 real wave vectors. In regions $E_1 < E < E_2$, $E_{-2} < E < E_{-1}$ we get 4 real wave vectors. We define that if k_x is positive corresponding to the energy region we focus on then we name it K-related wave vector, contrary to K related wave vector if k_x is negative then we name it K'-related wave vector. And We define right-going wave vector as p left-going wave vector as q respectively. Here the valley index was accompany with momentum $p^{(\tau)}$, we define $p^{(1)}, q^{(1)}$ ($p^{(2)}, q^{(2)}$) as $K\,(K')$ valley. X-axis is momentum k_x in unit of $K = \frac{4\pi}{3\sqrt{3}a}$;Y-axis is energy in unit of $t_0 = 2.66ev$

$$E_1 = \sin(k_y a_y), E_2 = \sqrt{5 - 4\cos(k_y a_y)}, E_3 = \sqrt{5 + 4\cos(k_y a_y)}, E_{-1} = -E_1 \;, E_{-2} = -E_2 \;, E_{-3} = -E_3$$

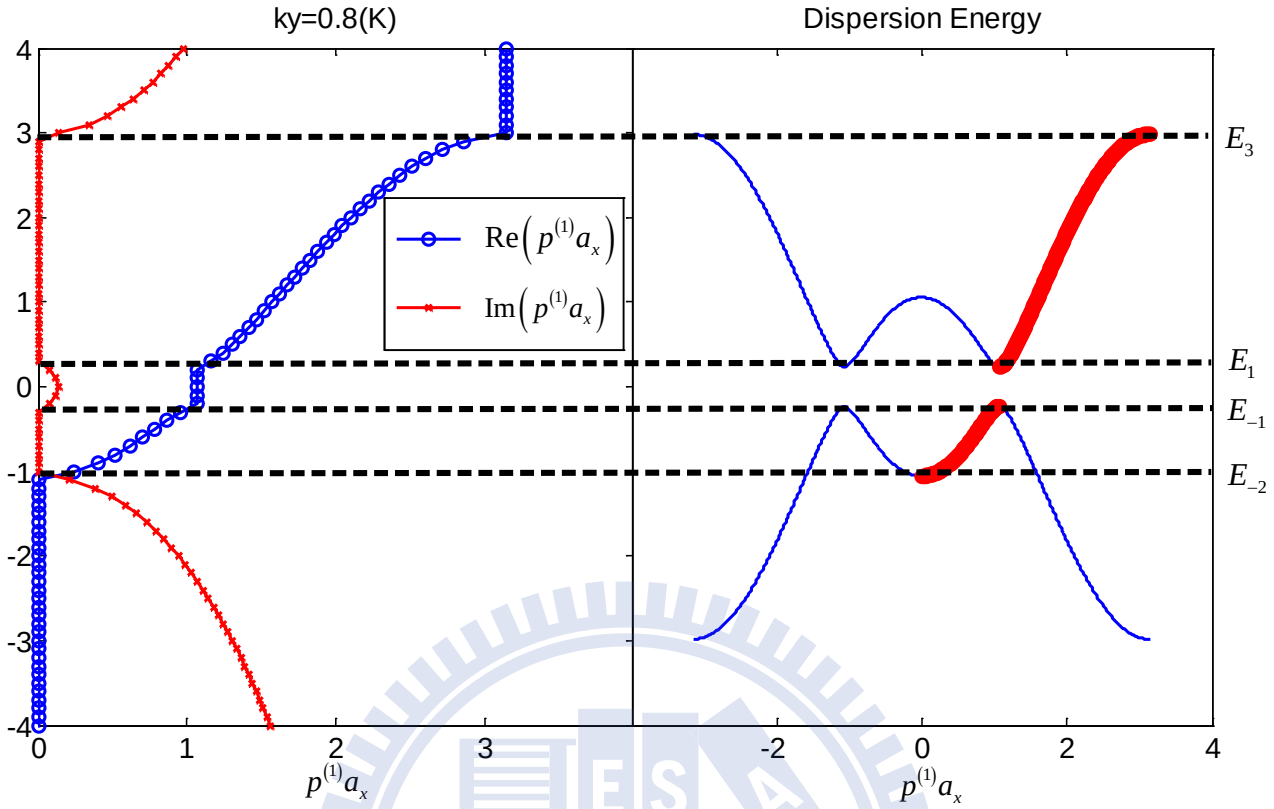

Fig.A.5 Left: Plot momentum $p^{(1)}$ in real(Blue circle) and imaginary(Red cross) part. Fix k_y at 0.8K. Right: Energy dispersion, which used to compare with the left figure. The red line label the momentum we are discussing. According to energy dispersion plot with red line, the group velocity is always positive. In regions $E > E_3$, $E < E_{-2}, E_{-1} < E < E_1$ $p^{(1)}$ is given by evanescent mode. In regions $E_1 \le E \le E_3, E_{-2} < E < E_{-1}$ $p^{(1)}$ is given by propagating mode. The imaginary part of $p^{(1)}$ become larger as the energy is further away from the band bottom, and become smaller as the energy is closer toward to the band bottom.

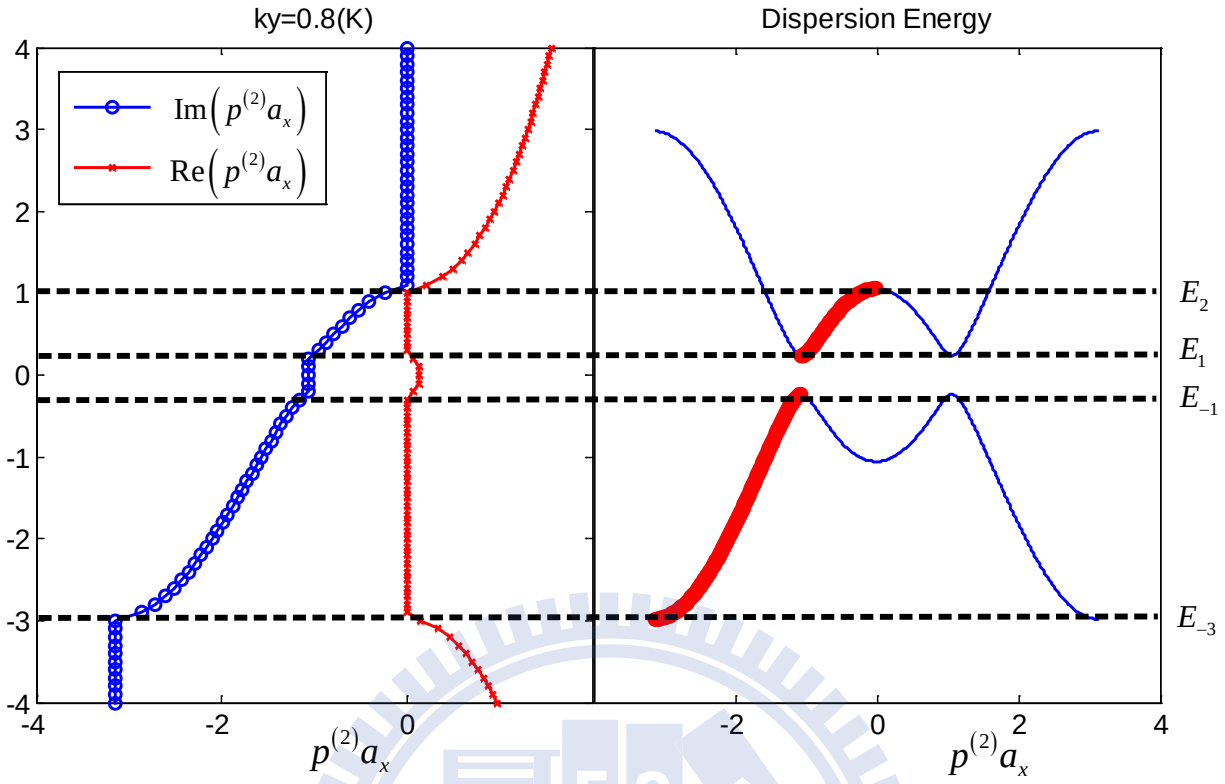

Fig.A.6 Left: Plot momentum $p^{(2)}$ in real(Blue circle) and imaginary(Red cross) part. Fix k_y at 0.8K. Right: Energy dispersion, which used to compare with the left figure. The red line label the momentum we are discussing. According to energy dispersion plot with red line, the group velocity is always positive. In regions $E > E_2$, $E < E_{-3}, E_{-1} < E < E_1$ $p^{(2)}$ is given by evanescent mode. In regions $E_1 \le E \le E_2, E_{-3} < E < E_{-1}, p^{(2)}$ is given by propagating mode. The imaginary part of $p^{(2)}$ become larger as the energy is further away from the band bottom, and become smaller as the energy is closer toward to the band bottom.

Appendix B

The current operator was defined as

$$j = \frac{\rho v + v\rho}{2} \tag{B.1}$$

Where ρ and v are density operator and velocity operator, respectively.

The density operator can be written down as

$$\rho = \frac{1}{a_0^{\,2}}\left[\left|M,N,A\right\rangle\left\langle M,N,A\right| + \left|M,N,B\right\rangle\left\langle M,N,B\right|\right] \tag{B.2}$$

a_0 is the lattice constant, on the other word it is the length between each lattices.

The velocity operator can be relevant to $[x,H]$

$$v = \frac{dx}{dt} = \frac{\left[x,\hat{H}\right]}{i} = \frac{1}{i}\left(x\hat{H} - \hat{H}x\right) \tag{B.3}$$

The Hamiltonian already introduce in Chapter 3

$$\hat{H} = -t_0 \sum_{M,N} \begin{bmatrix} \left|M+1\ ,N+1,A\right\rangle\left\langle M,N,B\right| \\ \left|M-1,N+1,A\right\rangle\left\langle M,N,B\right| \\ \left|\ \ M\ \ ,\ \ N\ \ ,A\right\rangle\left\langle M,N,B\right| \\ \left|M+1,N-1,B\right\rangle\left\langle M,N,A\right| \\ \left|M-1,N-1,B\right\rangle\left\langle M,N,A\right| \\ \left|\ \ M\ \ ,\ \ N\ \ ,B\right\rangle\left\langle M,N,A\right| \end{bmatrix} \tag{B.4}$$

The position operator is defined as

$$x = \sum_{M',N'} \begin{Bmatrix} \boldsymbol{R}_{M',N'}\left[\left|M'N'A\right\rangle\left\langle M'N'A\right| + \left|M'N'B\right\rangle\left\langle M'N'B\right|\right] \\ +\boldsymbol{d}\left|M'N'D\right\rangle\left\langle M'N'D\right| \end{Bmatrix} \tag{B.5}$$

In Eqn.(B.4), $\boldsymbol{R}_{M',N'}$ identify the position from subblattice A and B. The distance between sublattice A and B is defined by $\boldsymbol{d}$. $\left|M\ N\ D\right\rangle\left\langle M\ N\ D\right|$ help us ensure the difference between subblattice A and B. it works out as the following.

$$\begin{cases} \left\langle M\ N\ D\middle|M\ N\ A\right\rangle = 0 \\ \left\langle M\ N\ D\middle|M\ N\ B\right\rangle = 1 \end{cases}$$

To make it more specify we can see **Fig.B.1**

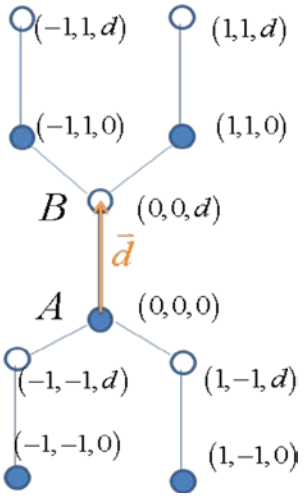

Fig.B.1 We set up sublattice A as original point and subblattice B is at a distance $\boldsymbol{d}$ away from A site. The coorinate here is described by capital $\boldsymbol{R}_{M,N,d}$

To make the current easier to obtain, we use δ_i to label the vectors we need to discuss.

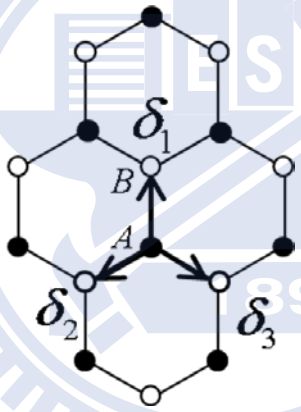

Fig.B.2 We define $\boldsymbol{\delta}_1,\boldsymbol{\delta}_2,\boldsymbol{\delta}_3$ as the vectors $(\boldsymbol{d}),(-\boldsymbol{a}_2+\boldsymbol{d}),(-\boldsymbol{a}_1+\boldsymbol{d})$ we will use later to present the current flow.

Now we can get commutation of $[x, H]$

$$[x,H] = -t_0 \sum_{M,N} \begin{bmatrix} -\delta_3 |M-1,N+1,A\rangle\langle M,N,B| \\ +\delta_3 |M+1,N+1,A\rangle\langle M,N,B| \\ -\delta_2 |M+1,N-1,B\rangle\langle M,N,A| \\ +\delta_2 |M-1,N-1,B\rangle\langle M,N,A| \\ -\delta_1 |M,N,A\rangle\langle M,N,B| \\ +\delta_1 |M,N,B\rangle\langle M,N,A| \end{bmatrix} \tag{B.6}$$

Combine (B.6) and (B.3) the velocity operator

$$v = -\frac{t_0}{i} \sum_{M,N} \begin{bmatrix} -\delta_3 |M-1,N+1,A\rangle\langle M,N,B| \\ +\delta_3 |M+1,N+1,A\rangle\langle M,N,B| \\ -\delta_2 |M+1,N-1,B\rangle\langle M,N,A| \\ +\delta_2 |M-1,N-1,B\rangle\langle M,N,A| \\ -\delta_1 |M,N,A\rangle\langle M,N,B| \\ +\delta_1 |M,N,B\rangle\langle M,N,A| \end{bmatrix} \tag{B.7}$$

Finally we get our current operator.

$$j = \frac{\rho v + v\rho}{2}$$

$$= \frac{-t_0}{2ia_0^{\,2}} \begin{Bmatrix} +\delta_3 \left[|M,N,A\rangle\langle M-1,N-1,B| + |M+1,N+1,A\rangle\langle M,N,B| \right] \\ -\delta_3 \left[|M,N,A\rangle\langle M+1,N-1,B| + |M-1,N+1,A\rangle\langle M,N,B| \right] \\ -\delta_2 \left[|M,N,B\rangle\langle M-1,N+1,A| + |M+1,N-1,B\rangle\langle M,N,A| \right] \\ +\delta_2 \left[|M,N,B\rangle\langle M+1,N+1,A| + |M-1,N-1,B\rangle\langle M,N,A| \right] \\ +2\delta_1 |M,N,B\rangle\langle M,N,A| - 2\delta_1 |M,N,A\rangle\langle M,N,B| \end{Bmatrix} \tag{B.8}$$

Bibliography

[1] A. K. Geim and K. S Novoselov, Nature Materials, **6,** 183 (2007)

[2] Claire Berger *et al*, Science, **312**, 1191 (2006);

[3] Changgu Lee and Xiaoding Wei, Science, **321,** 5887 (2008)

[4] O. Klein, Z. Physik, **53,** 157 (1926)

[5] M. I. Katsnelson, K. S. Novoselovand A. K. Geim, Nature Physics **2**, 620 - 625 (2006)

[6] B. Trauzettel, Ya. M. Blanter, and A. F. Morpurgo, Rev. B **75,** 035305 (2007)

[7] E. Perfetto, G. Stefanucci, and M. Cini1, Rev. B **82**, 035446 (2010)

[8] Zhenghao Gu, H. A. Fertig, Daniel P. Arovas, and Assa Auerbach, Rev. Lett **107**, 216601 (2011)

[9] Andrea F. Young and Philip Kim, Nature Physics **5**, 222 - 226 (2009)

[10] L. Brey, H. A. Fertig, Rev. Lett **103**, 046809 (2011)

[11] N. Stander, B. Huard, and D. Goldhaber-Gordon, Rev. Lett **102,** 026807 (2009)

[12] M. Tahir, K. Sabeeh and M. Ahsan Zeb,Phyx. Rev. B **78,** 165420 (2008)

[13] P. E. Tien and J. P. Gordon Phys. Rev. **129**, 647–651 (1963)